

## Lithospheric anisotropy beneath the Pyrenees from shear wave splitting

Guilhem Barruol, Annie Souriau, Alain Vauchez, Jordi Diaz, Josep Gallart,  
José Tubia, Julia Cuevas

► **To cite this version:**

Guilhem Barruol, Annie Souriau, Alain Vauchez, Jordi Diaz, Josep Gallart, et al.. Lithospheric anisotropy beneath the Pyrenees from shear wave splitting. *Journal of Geophysical Research: Solid Earth*, American Geophysical Union, 1998, 103 (B12), pp.30039 - 30053. <10.1029/98JB02790>. <hal-01388841>

**HAL Id: hal-01388841**

**<http://hal.univ-reunion.fr/hal-01388841>**

Submitted on 27 Oct 2016

**HAL** is a multi-disciplinary open access archive for the deposit and dissemination of scientific research documents, whether they are published or not. The documents may come from teaching and research institutions in France or abroad, or from public or private research centers.

L'archive ouverte pluridisciplinaire **HAL**, est destinée au dépôt et à la diffusion de documents scientifiques de niveau recherche, publiés ou non, émanant des établissements d'enseignement et de recherche français ou étrangers, des laboratoires publics ou privés.

# Lithospheric anisotropy beneath the Pyrenees from shear wave splitting

Guilhem Barruol,<sup>1</sup> Annie Souriau,<sup>2</sup> Alain Vauchez,<sup>1</sup> Jordi Diaz,<sup>3</sup> Josep Gallart,<sup>3</sup>  
José Tubia,<sup>4</sup> and Julia Cuevas<sup>4</sup>

**Abstract.** We investigate upper mantle anisotropy beneath the Pyrenean range along three N-S profiles across the mountain belt. The results of a first profile that operated in 1993 in the central part of the belt have been presented elsewhere. We present the results of two other profiles that ran in 1995-1996 and 1996-1997 in the eastern and western part of the belt, respectively and propose an interpretation of the whole results. Teleseismic shear waves (*SKS*, *SKKS*, and *PKS*) are used to determine splitting parameters: the fast polarization direction  $\phi$  and the delay time  $\delta t$ . Teleseismic shear wave splitting in the eastern Pyrenees displays homogeneous  $\phi$  values trending N100°E and  $\delta t$  values in the range 1.1 to 1.5 s. A station located in the southern Massif Central, 100 km north of the range, is characterized by different splitting parameters ( $\phi = \text{N}70^\circ\text{E}$ ,  $\delta t = 0.7$  s). In the western part of the belt, anisotropy parameters are similar across the whole belt ( $\phi = \text{N}110^\circ\text{E}$  and  $\delta t = 1.3$  to 1.5 s). Most of the measured delay times, including those obtained in the central part of the range, are above the global average of the *SKS* splitting (around 1 s). At the belt scale,  $\phi$  is generally poorly correlated with recent estimations of the absolute plate motion, which predicts a fast direction ranging between N50°E and N80°E. Instead, the orientation of  $\phi$  (N100°E) is parallel to the trend of the Pyrenean belt but also to Hercynian preexisting structures. This parallelism supports an anisotropy primarily related to frozen or active lithospheric structures. We show that a signature related to the Pyrenean orogeny is likely for the stations located in the internal domains of the belt. By contrast, the anisotropy measured at the stations located on the external parts of the belt could reflect a pre-Pyrenean (Hercynian) deformation. We suggest that a late Hercynian strike-slip deformation is responsible for this frozen upper mantle anisotropy and that the Pyrenean tectonic fabric developed parallel to this preexisting fabric. Finally, no particularly strong splitting is related to the North Pyrenean Fault, commonly believed to represent the plate boundary between Iberia and Eurasia.

## 1. Introduction

Although rock physics indicates that lithospheric behavior is primarily controlled by its upper mantle constituent, our knowledge of plate tectonics mainly derives from surface geology and crustal structures inferred from geophysical data. This last decade, however, shear wave splitting has been used as a mean to fill this gap. From indirect investigation of pervasive upper mantle structures [see *Silver*, 1996, and references herein], seismic anisotropy has become a new tectonic tool to characterize upper mantle flow. Seismic anisotropy at great depth is indeed broadly accepted to result from intrinsic elastic anisotropy of rock-forming minerals and from their preferred orientations developed in response to tectonic flow. Olivine, which represents

the main upper mantle constituent and which is the most anisotropic peridotite phase, controls upper mantle anisotropy [Nicolas and Christensen, 1987]. Since shear wave splitting is a direct result of anisotropy, and hence rock deformation, it is possible to investigate deep structure in relation to plate tectonics, in particular, beneath plate boundaries and mountain belts, where strong upper mantle deformations are expected to occur.

The Pyrenees result from an Albian-Cenomanian strike-slip motion of Iberia relative to Eurasia, followed by an Eocene collision between the two plates [e.g., Choukroune, 1992; Olivet, 1996]. The belt, oriented roughly E-W, exhibits a nearly cylindrical symmetry with several units (Figure 1): the Pyrenean Axial Zone is made of Paleozoic rocks and displays pervasive structures formed during the Hercynian orogeny. It is bounded northward by the North Pyrenean Fault (NPF), thought to represent the plate boundary in pre-Albian times. North of this fault, the North Pyrenean Zone (NPZ) is primarily composed of deformed Mesozoic rocks, which incorporate small Hercynian massifs and lherzolite bodies. The North Pyrenean Zone overthrusts the Aquitaine basin to the north. The NPZ structure is the consequence of the opening of the bay of Biscay and the related rotation of Iberia with respect to Eurasia 100 Myr ago: These events created a rift zone at the present location of the North Pyrenean Zone [e.g., Choukroune, 1992], which favored high-temperature and low-pressure metamorphism [Golberg and Leyreloup, 1990] and lherzolite emplacement [Vielzeuf and

<sup>1</sup>Laboratoire de Tectonophysique, CNRS, Université Montpellier II, Montpellier, France.

<sup>2</sup>Laboratoire de Dynamique Terrestre et Planétaire, CNRS, 14 av Belin, 31055 Toulouse, France.

<sup>3</sup>Institut de Ciències de la Terra, CSIC, Barcelona, Spain.

<sup>4</sup>Departamento de Geodinámica, Universidad del País Vasco, Bilbao, Spain.

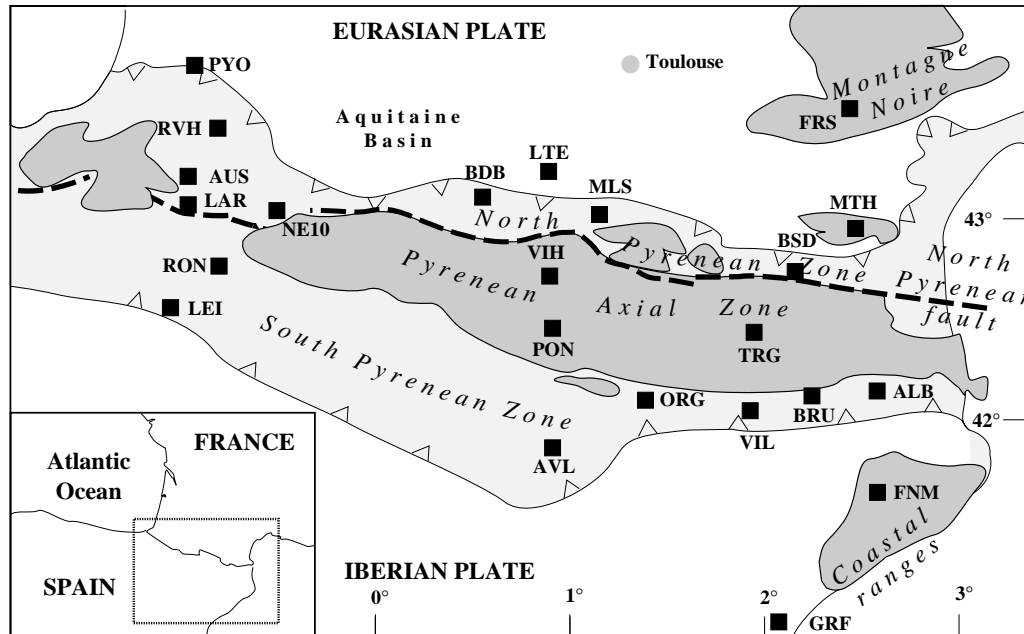


**Figure 1.** General map of the Pyrenees showing the tectonic units and the station locations.

Kornprobst, 1984]. South of the Paleozoic Axial Zone, the South Pyrenean Zone is made of Mesozoic and Cenozoic sedimentary nappes overthrusting the Ebro basin to the south.

Since teleseismic shear wave splitting is a marker of upper mantle tectonic fabric, our aim is to give some insights into the deep structures of the Pyrenees and to investigate the influence on seismic anisotropy of the various tectonic episodes that occurred in the Pyrenees. We focus our discussion on the upper mantle accommodation of the relative strike-slip motion and collision between the plates, on the signature of the North Pyrenean Fault and also on the departure of the belt from cylindrical symmetry. The role of present-day tectonics and the influence of preexisting structures is also discussed.

## 2. Data and Results

Teleseismic events were recorded during three experiments along N-S profiles (see station location Figure 1): the first experiment described by *Barruol and Souriau* [1995] ran in 1993 in the central part of the belt; the second experiment ran in 1995–1996 across the eastern Pyrenees, and the third one ran in 1996–1997 in the western part of the belt.

For the eastern experiment, eight broadband three components seismic stations from the French LITHOSCOPE network were installed between the southern Massif Central (France) and Barcelona (Spain). Four additional stations from the Institute of Earth Sciences from Barcelona were installed for a few months on the Spanish side of the belt, either at sites later occupied by LITHOSCOPE stations (ORG and ALB) or at sites in the Catalan coastal ranges (BRU and FNM). These stations provide anisotropy measurements laterally off the N-S profile (see Table 1 for the station location). The experiment ran between January 1995 and April 1996. Continuous recording at 15 samples per second with Lennartz 5 s sensors allowed us to select and extract teleseismic events of convenient distances and magnitudes suitable for SKS, SKKS and PKS splitting measurements. From the whole data set of teleseismic events located at a distance greater than  $85^\circ$  and

magnitude greater than 5.8, about 40 events were kept after visual inspection (Table 2). In order to avoid noise contamination of the splitting measurements, only events characterized by signal to noise ratio of the SKS phase higher than 2 were kept.

For the western profile, six broadband or intermediate period, three-component stations from the LITHOSCOPE network and from the Pyrenean seismic survey network were installed during the period July 1996 to May 1997. Unfortunately, these stations did not record continuously, and due to small data storage capacity, a rather high threshold in record triggering was used. Moreover, the proximity of the Atlantic Ocean induces a high level of microseismic noise. This explains the smaller number of events obtained during this experiment.

The splitting of seismic shear waves is a direct effect of seismic anisotropy: If one excepts the case where the incidence plane is coincident with one of the polarization plane, a polarized shear wave crossing an anisotropic medium is split into two perpendicularly polarized waves that propagate at different velocities. Anisotropy parameters may be retrieved from three-component seismic records: the difference in arrival time ( $\delta t$ ) between the two split waves, which depends on the thickness and intrinsic anisotropy of the anisotropic medium, and the orientation of the split waves polarization planes ( $\phi$  for the fast wave), which are related to the orientation of the structure. The shear wave splitting measurements were obtained using the *Silver and Chan* [1991] algorithm. This method assumes a hexagonal symmetry of anisotropy with a horizontal symmetry axis and determines the anisotropy parameters,  $\phi$  and  $\delta t$ , that best removes energy on the transverse component of the seismogram for a selected time window. Some examples of splitting measurements are shown Figure 2. Despite the small number of measurements performed in western Pyrenees, event 97023 recorded at AUS and LEI provides an example of a well constrained result. Event 95291 in eastern Pyrenees (TRG) and southern Massif Central (FRS) gives a less constrained measurement but clearly shows a different signature between the two areas.

The event origins and locations (Table 2) are taken from the

**Table 1.** Station Locations, Mean Splitting Parameters with  $1\sigma$  errors

| Station | Latitude,<br>°N | Longitude,<br>°E | Elevation,<br>m | $\phi$ ,<br>deg | $\sigma\phi$ ,<br>deg | $\delta t$ ,<br>s | $\sigma \delta t$ ,<br>s | Number of<br>Measurements |
|---------|-----------------|------------------|-----------------|-----------------|-----------------------|-------------------|--------------------------|---------------------------|
| FRS     | 43.365          | 2.447            | 860             | 75              | 4                     | 0.70              | 0.10                     | 6                         |
| MTH     | 42.939          | 2.534            | 620             | 102             | 2                     | 1.29              | 0.09                     | 11                        |
| BSD     | 42.795          | 2.156            | 1110            | 97              | 4                     | 1.12              | 0.11                     | 10                        |
| TRG     | 42.502          | 1.967            | 1520            | 99              | 3                     | 1.45              | 0.09                     | 15                        |
| ALB     | 42.314          | 2.721            | 120             | 101             | 6                     | 1.80              | 0.21                     | 6                         |
| ORG     | 42.227          | 1.332            | 998             | 101             | 4                     | 0.98              | 0.16                     | 3                         |
| VIL     | 42.136          | 1.891            | 795             | 89              | 3                     | 1.07              | 0.08                     | 19                        |
| GRF     | 41.152          | 1.891            | 280             | 86              | 2                     | 1.75              | 0.11                     | 14                        |
| FNM     | 41.762          | 2.433            | 222             | 120             | 5                     | 1.25              | 0.18                     | 1                         |
| BRU     | 42.283          | 2.186            | 223             | 96              | 5                     | 0.93              | 0.01                     | 3                         |
| PYO     | 43.538          | -0.880           | 180             | 112             | 5                     | 1.45              | 0.28                     | 1                         |
| RVH     | 43.348          | -0.847           | 160             | 110             | 2                     | 1.45              | 0.23                     | 1                         |
| AUS     | 43.152          | -0.933           | 210             | 110             | 5                     | 1.25              | 0.03                     | 3                         |
| LAR     | 43.023          | -0.938           | 540             | 116             | 3                     | 1.39              | 0.13                     | 3                         |
| RON     | 42.797          | -0.964           | 470             | 102             | 4                     | 1.45              | 0.12                     | 2                         |
| LEI     | 42.652          | -1.220           | 250             | 105             | 4                     | 1.48              | 0.14                     | 2                         |

U.S. Geological Survey (USGS) Preliminary Determination of Epicenters, and the phase arrivals were computed using the IASP91 Earth reference model [Kennett, 1995]. Most individual measurements were performed on earthquakes occurring at distances in the range 85 to 115°. The *SKS* phase was generally used, but for some events, the whole *SKS* + *SKKS* wave train was selected. For some events occurring at distances between 130 and 140°, *PKS* and *SKKS* phases gave good results (event 95226, for instance). Many events do not show any evidence of signal on the transverse component. Such events, are classically considered as "null" results and indicate either that there is no anisotropy beneath the station or that the initial polarization direction of the *SKS* wave is parallel to the fast or slow direction in the anisotropic layer. This second possibility is the only considered when non-null measurements are obtained at the same station. These null results are also shown in Figure 3, on the right. Table 3 summarizes the individual splitting parameters. For each, we report the split phase on which the measurement has been performed, the distance and backazimuth of the event, and the splitting parameters ( $\phi$ ,  $\delta t$ ) with their  $1\sigma$  uncertainty, determined from the 95% confidence interval in the ( $\phi$ - $\delta t$ ) domain. We also ascribe a quality factor (good, fair, or poor) to the measurements depending on the signal to noise ratio of the initial phase, the rectilinear polarization of the particle motion in the horizontal plane after anisotropy correction, and the wave form correlation between the fast and slow split shear waves. This evaluation of the quality is particularly useful in temporary experiments, when relatively few data are available. Few individual measurements were performed on earthquakes occurring at distances less than 85°. Event 95231, occurring at a distance of about 78° is one of the exceptions: at this distance, and given the depth of this event (125 km), the *sSKS* phase arrives after the *S*, *ScS*, and *sS* phases. Splitting measurements on such *sSKS* phases have been done with confidence because the *S* and *ScS* phases were impulsive and did not appear to contaminate the following *sSKS* phase. A second exception is event 97084, at a distance of 82°. Since this event is very deep (609 km), we assumed that the splitting occurs primarily beneath the station and not at the source and used the

direct *S* wave to characterize the anisotropy.

A strikingly large difference in the number of splitting measurements appears between the eastern and the western stations (Figure 3). This is mainly related to two factors: the eastern experiment ran for a much longer time (16 months as compared to 10 months in the western Pyrenees) and also continuous recording strongly increased the number of available data. It appears from Figure 3 and Table 3 that good measurements at a given site may display some variations in splitting parameters (10 to 20° in azimuth and 0.1 to 0.2 s in delay time); this may result from lateral heterogeneities, but this may also indicate that the initial assumptions used for calculations are not fulfilled, that is, that several layers of anisotropy exist beneath the station and/or that the anisotropy symmetry axis is dipping. Such structures should result in an apparent variation of the splitting parameters correlated with the event backazimuth, with a periodicity of  $\pi/2$  and  $\pi$ , respectively [Savage and Silver, 1993; Silver and Savage, 1994]. No such systematic variation is clearly detected, but the amount of data obtained during the temporary experiments is too small to allow a confident characterization of such properties. In most cases, however (if we except FRS, see discussion below), 95% confidence intervals overlap in the  $\phi$ - $\delta t$  plot, and individual splitting measurements display a coherent pattern of nulls and non nulls, suggesting a model of anisotropy dominated by a single anisotropic layer.

We test the dependence of the splitting parameters on the signal frequency because it may give some insights on the degree of heterogeneity of the anisotropic layer and on the lateral or radial variations of the structures [Marson-Pidgeon and Savage, 1997]. On few constrained events (97023 at LEI and AUS and 95291 at TRG), we used the method from Marson-Pidgeon and Savage [1997] in which the splitting parameters are analyzed as a function of the dominant period of the split phase. We filtered the signal using narrow band-pass filters and determined the corresponding splitting parameters. By slightly moving the band-pass window in the frequency domain, we investigated possible variations in the  $\phi$ - $\delta t$  parameters as a function of the dominant

**Table 2.** Events used for SKS splitting measurements

| Event | Date           | Time, UT   | Latitude,<br>°N | Longitude,<br>°E | Depth<br>,<br>km | $m_b$ |
|-------|----------------|------------|-----------------|------------------|------------------|-------|
| 95006 | Jan. 6, 1995   | 22 37:37.9 | 40.227          | 142.242          | 57               | 6.7   |
| 95016 | Jan. 16, 1995  | 18 14:49.4 | 51.241          | 179.172          | 33               | 5.5   |
| 95021 | Jan. 21, 1995  | 08 47:29.9 | 43.335          | 146.717          | 63               | 6.5   |
| 95036 | Feb. 5, 1995   | 22 51:10.4 | -37.714         | 178.769          | 59               | 6.4   |
| 95045 | Feb. 14, 1995  | 20 47:41.1 | 43.991          | 148.098          | 37               | 5.9   |
| 95090 | March 31, 1995 | 14 01:40.8 | 38.150          | 135.058          | 365              | 6.0   |
| 95107 | April 17, 1995 | 23 28:08.3 | 45.904          | 151.288          | 34               | 6.1   |
| 95111 | April 21, 1995 | 00 09:56.2 | 11.999          | 125.699          | 33               | 6.1   |
| 95111 | April 21, 1995 | 00 30:12.9 | 11.902          | 125.568          | 33               | 6.3   |
| 95113 | April 23, 1995 | 05 08:03.2 | 12.377          | 125.364          | 33               | 6.0   |
| 95118 | April 28, 1995 | 16 30:00.7 | 44.058          | 148.055          | 29               | 6.6   |
| 95119 | April 29, 1995 | 09 44:00.3 | 11.766          | 126.044          | 33               | 5.4   |
| 95125 | May 5, 1995    | 03 53:47.6 | 12.622          | 125.314          | 33               | 6.2   |
| 95128 | May 8, 1995    | 18 08:09.6 | 11.567          | 125.900          | 33               | 5.6   |
| 95143 | May 23, 1995   | 22 10:11.3 | -56.097         | -3.150           | 10               | 5.3   |
| 95175 | June 24, 1995  | 06 58:06.5 | -3.979          | 153.945          | 386              | 6.2   |
| 95180 | June 29, 1995  | 07 45:09.7 | 48.784          | 154.459          | 62               | 5.9   |
| 95180 | June 29, 1995  | 12 24:03.9 | -19.464         | 169.241          | 144              | 6.2   |
| 95181 | June 30, 1995  | 11 58:56.4 | 24.621          | -110.264         | 10               | 5.8   |
| 95193 | July 12, 1995  | 15 46:59.8 | -23.237         | 170.824          | 33               | 5.9   |
| 95208 | July 27, 1995  | 05 51:17.9 | -12.578         | 79.237           | 10               | 6.2   |
| 95211 | July 30, 1995  | 05 11:23.5 | -23.364         | -70.312          | 47               | 6.6   |
| 95215 | Aug. 3, 1995   | 01 57:21.7 | -23.132         | -70.602          | 33               | 5.4   |
| 95226 | Aug. 14, 1995  | 04 37:17.3 | -4.827          | 151.507          | 126              | 6.3   |
| 95231 | Aug. 19, 1995  | 21 43:32.4 | 5.096           | -75.690          | 125              | 6.1   |
| 95235 | Aug. 23, 1995  | 07 06:02.6 | 18.857          | 145.186          | 596              | 6.3   |
| 95257 | Sept. 14, 1995 | 14 04:31.6 | 16.844          | -98.599          | 21               | 6.4   |
| 95262 | Sept. 19, 1995 | 03 31:53.6 | -21.228         | -68.740          | 110              | 5.7   |
| 95266 | Sept. 23, 1995 | 22 31:58.3 | -10.529         | -78.697          | 73               | 5.9   |
| 95279 | Oct. 6, 1995   | 18 09:45.9 | -2.089          | 101.414          | 33               | 5.8   |
| 95291 | Oct. 18, 1995  | 10 37:26.3 | 27.920          | 130.337          | 27               | 6.5   |
| 95292 | Oct. 19, 1995  | 00 32:06.4 | 28.145          | 130.206          | 33               | 5.9   |
| 95305 | Nov. 1, 1995   | 00 35:32.3 | -28.958         | -71.503          | 20               | 6.3   |
| 95312 | Nov. 8, 1995   | 07 14:18.5 | 1.853           | 95.062           | 33               | 6.1   |
| 95328 | Nov. 24, 1995  | 17 24:12.5 | 44.542          | 149.091          | 33               | 6.1   |
| 95331 | Nov. 27, 1995  | 15 52:58.3 | 44.519          | 149.137          | 33               | 6.0   |
| 95334 | Nov. 30, 1995  | 23 37:37.4 | 44.341          | 149.403          | 33               | 5.9   |
| 95336 | Dec. 2, 1995   | 17 13:18.7 | 44.490          | 149.342          | 19               | 6.0   |
| 95337 | Dec. 3, 1995   | 18 01:08.7 | 44.575          | 149.390          | 33               | 6.7   |
| 95345 | Dec. 11, 1995  | 14 09:23.9 | 18.785          | -105.505         | 33               | 5.7   |
| 95359 | Dec. 25, 1995  | 04 43:24.9 | -6.943          | 129.179          | 150              | 6.2   |
| 96001 | Jan. 1, 1996   | 08 05:11.9 | 0.724           | 119.981          | 33               | 6.2   |
| 96038 | Feb. 7, 1996   | 21 36:45.1 | 45.321          | 149.909          | 33               | 6.3   |
| 96047 | Feb. 16, 1996  | 15 22:57.8 | 37.343          | 142.474          | 33               | 6.2   |
| 96053 | Feb. 22, 1996  | 14 59:09.7 | 45.208          | 148.557          | 133              | 6.2   |
| 96065 | March 5, 1996  | 14 52:28.6 | 24.092          | 122.215          | 30               | 6.1   |
| 96077 | March 17, 1996 | 14 48:56.7 | -14.705         | 167.297          | 164              | 5.8   |
| 96082 | March 22, 1996 | 03 24:20.0 | 51.221          | 178.695          | 20               | 5.7   |
| 96090 | March 30, 1996 | 13 05:17.4 | 52.214          | -168.734         | 33               | 5.9   |
| 96107 | April 16, 1996 | 00 30:54.6 | -24.061         | -177.036         | 111              | 6.4   |
| 96198 | July 16, 1996  | 10 07:36.6 | 1.016           | 120.254          | 33               | 6.0   |
| 96204 | July 22, 1996  | 14 19:35.7 | 1.000           | 120.450          | 33               | 6.0   |
| 96249 | Sept. 5, 1996  | 23 42:06.1 | 21.898          | 121.498          | 20               | 6.4   |
| 96255 | Sept. 11, 1996 | 02 37:14.9 | 35.537          | 140.943          | 55               | 6.1   |
| 96293 | Oct. 19, 1996  | 08 31:49.8 | 31.840          | 131.804          | 33               | 5.4   |
| 96310 | Nov. 5, 1996   | 09 41:34.7 | -31.160         | 179.998          | 369              | 5.9   |
| 96357 | Dec. 22, 1996  | 14 53:27.6 | 43.207          | 138.920          | 227              | 6.0   |
| 97023 | Jan. 23, 1997  | 02 15:22.9 | -21.999         | -65.719          | 276              | 6.4   |
| 97084 | March 25, 1997 | 16 44:32.5 | -9.090          | -71.320          | 603              | 5.4   |
| 97145 | May 25, 1997   | 23 22:33.8 | -31.980         | 179.700          | 333              | 7.1   |
| 97149 | May 29, 1997   | 17 02:38.7 | -35.964         | -102.511         | 10               | 5.6   |

signal frequency. No significant variation of the parameters is observed, suggesting rather homogeneous anisotropic structures. However, the sensors band pass (0.1-10 Hz) impedes investigation on a broad range of periods, which could allow more reliable conclusions on the upper mantle heterogeneity.

The general coherency of the results allowed us to calculate the mean splitting parameters at each site. We used the averaging method presented by *Silver and Chan* [1991], which weights each individual measurement by its 95% confidence interval (reported in Table 3), so that poorly constrained results are have only a small contribution to the mean result. In order to test the validity of the result, we determined the mean splitting parameters ( $\phi$ ,  $\delta t$ ) using three sets of data: (1) the whole set of measurements, (2) only good and fair measurements, and finally, (3) good measurements only. The results obtained from the three different data sets are consistent:  $\phi$  and  $\delta t$  variations do not exceed  $\pm 5^\circ$  and  $\pm 0.1$  s, respectively. Therefore the mean splitting results presented in Table 1 and plotted in Figure 4 are based on the whole data set. GRF is the only station at which large variations in  $\delta t$  are observed depending on the averaged data:  $\delta t$  decreases from 1.75 s for the whole data set (14 measurements) to 1.56 s when four poor measurements with very high  $\delta t$  (above 2.0 s) are removed.

In the eastern part of the belt, most of the stations are characterized by a fast direction  $\phi$  trending N90°E to N100°E and by rather high  $\delta t$  values in the range 1.0 to 1.7 s (see Table 1 and Figure 4). These results are generally well constrained by numerous splitting measurements. Except at station ORG, FNM, and BRU, average splitting parameters are calculated from more than five individual measurements and often from more than 10 measurements. No systematic variation of  $\delta t$  is observed across the belt, and particularly across the NPF, as in the central Pyrenees, indicating the absence of significant lateral variations in the anisotropy magnitude at depth. The  $\phi$  trend observed at FNM in the Coastal Ranges (N120°E) seems to be slightly different than at the other stations, but it derives from a single measurement. No particularly strong  $\delta t$  is found at BSD, the station located close to the North Pyrenean Fault. Anisotropy in the southern Massif Central clearly contrasts with the rest of the profile, in trend, magnitude but also in quality. At FRS, the azimuth of the fast split shear wave trends around N75°E, the delay time seems to be significantly smaller than at the other stations (around 0.7 s), and some nulls are inconsistent with non-null splitting measurements. This pattern may be related to complex upper mantle structure beneath this station, such as dipping structures, heterogeneities, or multiple anisotropic layers.

In the western part of the belt, although the results derive from a much smaller data set, some high-quality events (see Figure 2) allow us to interpret the final results with confidence. The most striking feature is the homogeneity of the results across the belt:  $\phi$  trends around N110°E and  $\delta t$  is homogeneously high, around 1.3 to 1.4 s. As in the eastern Pyrenees, no specific anisotropy signature is observed at the station closest to the NPF (LAR).

The anisotropy study in the central Pyrenees [*Barruol and Souriau*, 1995] led to the main following results: (1) the anisotropy in the Pyrenean units belonging to the Iberian plate is homogeneous with splitting parameters,  $\phi \approx$  N100°E and  $\delta t$  in the range 1.3 to 1.5 s. (2) North from the NPF, anisotropy in the North Pyrenean Zone is characterized by varying  $\phi$  (from N70°E to E-W) and smaller  $\delta t$  (0.6 to 1.0 s).

Splitting measurements obtained from the three profiles,

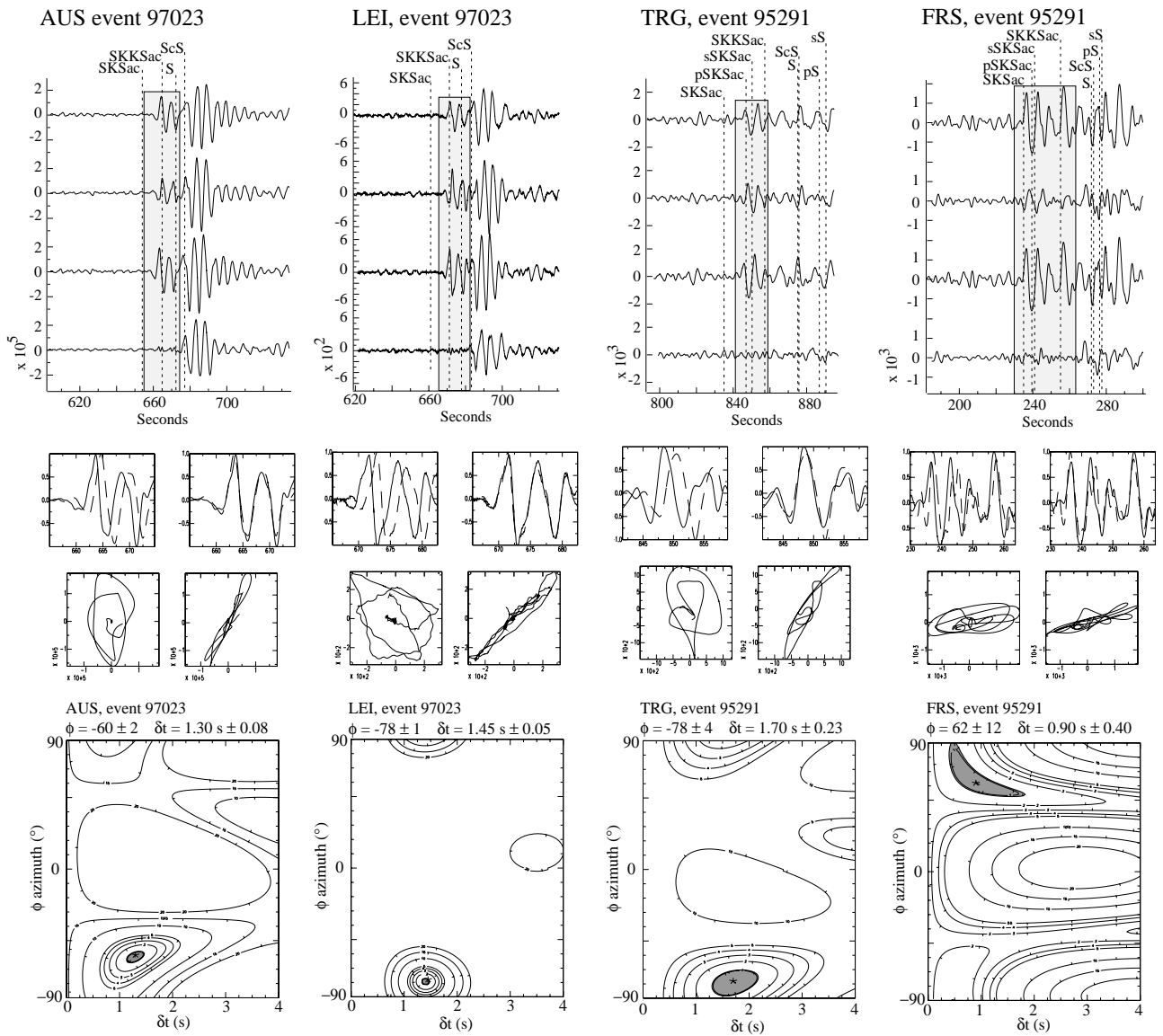
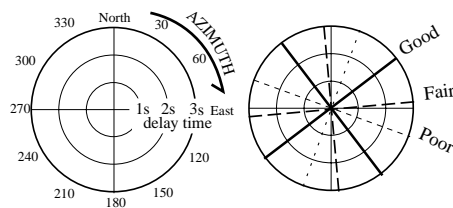
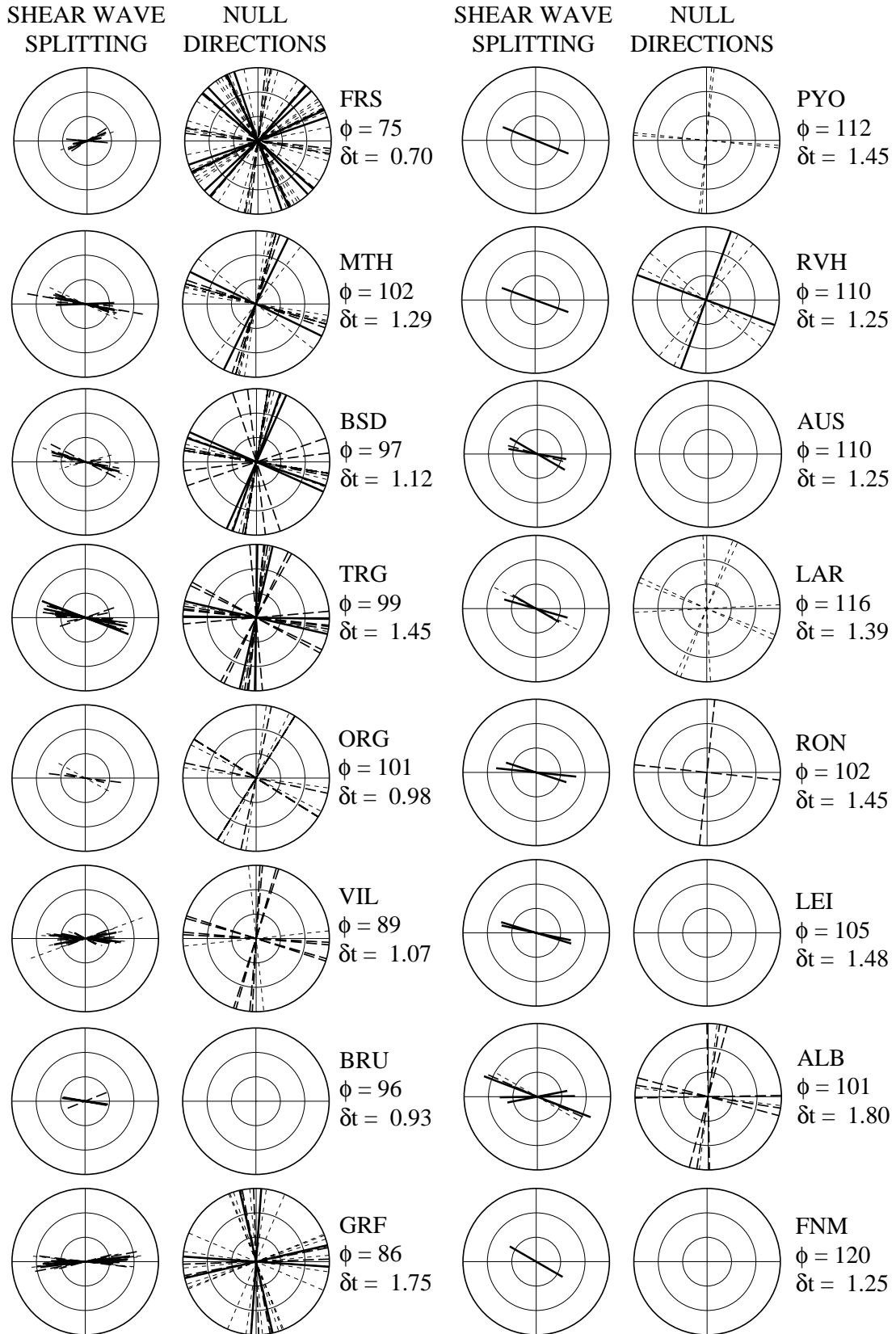


**Figure 2.** Examples of splitting measurements at four stations: *SKS* phase for event 97023 (see location on Table 2), recorded at two stations from the western Pyrenees (AUS and LEI) on both sides of the North Pyrenean Fault, and event 95291, recorded at two stations from the eastern experiment, one in the axial zone (TRG) and the other in the southern Massif Central (FRS). (top) For each station we show two upper traces, the initial radial and transverse components (note the energy on the transverse component), and two lower traces, the same traces corrected for anisotropy (there is no longer energy on the transverse component). The vertical dashed lines represent the predicted phase arrival times from the IASP91 Earth model. The shaded area gives the time window on which the splitting measurement is done. (middle) Four plots of the fast and slow components (continuous and dashed lines, respectively) of the split shear waves, (left) raw and (right) corrected for the best calculated delay time. Particle motions in the horizontal plane are shown below, also (left) uncorrected and (right) corrected for the anisotropy: the elliptical particle motion becomes rectilinear when the anisotropy is corrected. (bottom) Contour plot of energy on the transverse component as a function of the delay time  $\delta t$  (seconds) and the polarization angle  $\phi$  (degrees) of the fast split shear wave. The shaded area represents the 95% confidence interval. This last diagram allows the determination of 95% confidence interval for the splitting parameters from which the  $1\sigma$  uncertainties are deduced.

together with those obtained at the NARS station NE10 [Souriau and Njike-Kassala, 1993], allow us to define some general characteristics: On the Iberian plate,  $\phi$  homogeneously trends around  $N100-110^\circ E$ , and  $\delta t$  is rather large, typically in the range 1.1 to 1.5 s. On the other hand, the abrupt variation in splitting parameters across the North Pyrenean Fault observed in the

central Pyrenees is not observed in the eastern and western portions of the belt. Instead,  $\phi$  is rather stable along the eastern profile (around  $N100^\circ E$ ) except for stations out of the range (FRS in the Massif Central and FNM in the Catalan Coastal ranges). Interestingly, GRF, also out of the range has one of the highest  $\delta t$  of the profile (1.75 s).



### 3. The Lithospheric Origin of the Anisotropy

Although it is widely accepted that a major part of the teleseismic shear wave splitting occurs in the upper mantle, the lack of vertical resolution in measurements of core shear waves splitting let open the investigations about the asthenospheric and/or lithospheric origin of the splitting. Inferences about the source regions of anisotropy and the processes that generate mantle deformation fabrics may be drawn through a comparison of anisotropy signatures expected from these processes and observed splitting parameters.

In the central Pyrenees, the short-scale variation of the anisotropy parameters and their correlation to the NPF, as well as the better correlation of the azimuth of the fast split direction with lithospheric structures rather than with absolute plate motion orientation, led *Barruol and Souriau* [1995] to suggest that the anisotropy is predominantly of lithospheric origin.

In light of the new data presented in this work, this discussion has to be updated. We first compare our observations with the anisotropy predicted from absolute plate motion (APM). Assuming a flat geometry of the lithosphere/asthenosphere boundary, asthenospheric drag beneath a lithospheric plate would result in  $\phi$  oriented parallel to the plate motion vector [*Tommasi et al.*, 1996; *Vinnik et al.*, 1992]. The HS2-Nuvell1 and NNR-Nuvell1 absolute plate motion models predict asthenospheric flow beneath the Pyrenees trending about N45°-N50°E [*DeMets et al.*, 1990; *Gripp and Gordon*, 1990]. These predictions, however, are poorly constrained for the Eurasian plate because of the very low velocity of this plate and because no local hot spot tracks were incorporated into the HS2-Nuvell1 model to constrain local APM. J. Morgan (personal communication, 1996) defined a model incorporating hot spot tracks on the Eurasian and African plates which gives a APM trending N80°E with a velocity of about 5 mm/yr in the Pyrenees. Excepted for the Massif Central station FRS, none of the measured fast polarization direction is close to the prediction for any model. The misfit reaches 20-30° using Morgan's APM and 50 to 60° using HS2-Nuvell1 APM. Second, short-wavelength variations in the splitting parameters found in several places in the eastern Pyrenees are hardly compatible with a deep source (deeper than 100 km) of anisotropy related to large-scale mantle shear flow. For instance, significant  $\delta t$  variations are observed between TRG ( $\delta t = 1.45$  s) and VIL ( $\delta t = 1.07$  s) less than 50 km apart. Third, the observed  $\phi$  directions correlate well with the outcropping lithospheric structures:  $\phi$ s parallel to the Pyrenean and Hercynian pervasive structures of the Pyrenees. Fourth, the largest  $\delta t$  are generally observed on the Iberian plate, which was found, from *P* wave residuals [*Poupinet et al.*, 1992], to have a thicker crust and lithosphere than the adjacent European plate. This apparent correlation of  $\delta t$  with lithospheric thickness is compatible with a lithospheric origin of the anisotropy. Fifth, it is also interesting to note that *Pn* tomography [*Granet et al.*, 1997] reveals a *P* wave anisotropy of about 4% trending roughly E-W in

the central and eastern Pyrenees. This fast *P* wave direction in the uppermost lithospheric mantle is compatible with our *SKS* splitting observations and clearly argue for a subcrustal, lithospheric anisotropy.

More complex asthenospheric models of forced flow around complex geometry of the lithosphere-asthenosphere boundary have been suggested [*Bormann et al.*, 1996] to integrate short-scale anisotropy variations in an asthenospheric mantle flow. The tomographic studies [*Souriau and Granet*, 1995], *P* residuals [*Poupinet et al.*, 1992] or electromagnetic soundings [*Pous et al.*, 1995] support the existence of a downward lithospheric bending of the Iberian lithosphere but do not give evidence of short-wavelength sublithospheric heterogeneities.

Observations in the eastern and western Pyrenees therefore strengthen the previous conclusions inferred from the central Pyrenees measurements, that is, that the anisotropy appears to correlate better with the uppermost mantle structures rather than with an asthenospheric flow beneath the plate. Obviously, this latter contribution cannot be reasonably rejected from our observations, but if present, it seems to be much smaller than the lithospheric effect.

### 4. Seismic Anisotropy and Deep Structures of the Belt

Considering that uppermost mantle structures dominates our shear wave splitting measurements in the Pyrenees, it is worth comparing our results to other geophysical data available for this belt. At the crustal scale, an asymmetric structure of the belt is well established by various methods, particularly for the central Pyrenees: balanced cross sections [*Séguret and Daignières*, 1986] show that the Iberian crust was much thicker than the Eurasian margin after the rotation of Iberia 107-90 Myr ago. This N-S crustal asymmetry is still present as imaged from seismic refraction profiles [*Daignières et al.*, 1982] and has been largely confirmed by the ECORS vertical seismic reflection experiment [*Roure and ECORS Pyrenees Team*, 1989]. In the central part of the range, the Iberian crust is 15 km thicker than the Eurasian crust.

The N-S asymmetry of the belt has also been imaged at lithospheric scale in the central Pyrenees. Interpretation of *P* travel time residuals [*Poupinet et al.*, 1992] confirms the large Moho vertical offset and also suggests an Iberian lithosphere thicker than the Eurasian one. The seismic tomography of the belt [*Souriau and Granet*, 1995] reveals, at upper mantle depths (between 50 and 100 km) beneath the Pyrenean Axial Zone (see Figure 5a), a prominent E-W trending low-velocity anomaly, contrasting with high velocities observed beneath the NPZ and Aquitaine Basin. This anomaly was interpreted as an incipient subduction of Iberian lower crust beneath the Eurasian plate. A similar conclusion was reached independently by *Pous et al.* [1995] from magnetotelluric soundings along a N-S profile in the

---

**Figure 3. (opposite)** Summary of (left) non-null and (right) null measurements at each station. For non-null measurements, the trend of each segment represents the azimuth of the fast split shear wave polarization plane, and its length is proportional to the delay time (up to 3.0 s). Solid lines correspond to well-constrained results, large dashed lines correspond to fair results, and small dashed lines correspond to poorly constrained results (as reported Table 3). For null measurements, we represents backazimuth (radial direction) of unsplit events. We also plot the perpendicular (transverse) direction that may correspond to the fast or slow direction in the anisotropic layer. For each station, we report the calculated splitting parameters.



**Table 3.** Results of Individual Splitting Measurements Obtained at Various Stations

| Station | Event | Distance,<br>deg | Back-<br>azimuth,<br>deg | $\phi$ ,<br>deg | $\sigma\phi$ ,<br>deg | $\delta t$ ,<br>s | $\sigma \delta t$ ,<br>s | Phase | Quality |
|---------|-------|------------------|--------------------------|-----------------|-----------------------|-------------------|--------------------------|-------|---------|
| FRS     | 95006 | 89               | 30                       | -84.            | -                     | -                 | -                        | SKS   | f       |
| FRS     | 95016 | 91               | 38                       | -26.            | -                     | -                 | -                        | SKS   | f       |
| FRS     | 95107 | 87               | 21                       | 40.             | -                     | -                 | -                        | SKS   | f       |
| FRS     | 95111 | 105              | 58                       | -84.            | 18.                   | 0.40              | 0.22                     | SKS   | f       |
| FRS     | 95113 | 104              | 58                       | 71.             | 7.                    | 1.15              | 0.32                     | SKS   | p       |
| FRS     | 95119 | 105              | 58                       | -26.            | -                     | -                 | -                        | SKKS  | f       |
| FRS     | 95175 | 133              | 41                       | -43.            | -                     | -                 | -                        | PKS   | g       |
| FRS     | 95180 | 154              | 29                       | -79.            | -                     | -                 | -                        | SKKS  | p       |
| FRS     | 95211 | 94               | 242                      | -33.            | -                     | -                 | -                        | SKS   | p       |
| FRS     | 95215 | 94               | 242                      | 65.             | -                     | -                 | -                        | SKS   | g       |
| FRS     | 95226 | 133              | 44                       | 78.             | 6.                    | 0.60              | 0.10                     | PKS   | g       |
| FRS     | 95228 | 135              | 42                       | 55.             | -                     | -                 | -                        | PKS   | p       |
| FRS     | 95266 | 91               | 256                      | 71.             | -                     | -                 | -                        | SKS   | g       |
| FRS     | 95291 | 94               | 44                       | 66.             | 11.                   | 0.85              | 0.30                     | SKS   | g       |
| FRS     | 95291 | 94               | 44                       | 57.             | 13.                   | 0.95              | 0.40                     | SKKS  | f       |
| FRS     | 95312 | 91               | 87                       | -80.            | -                     | -                 | -                        | SKS   | f       |
| FRS     | 95337 | 88               | 23                       | -49.            | -                     | -                 | -                        | SKS   | g       |
| FRS     | 96064 | 93               | 53                       | 60.             | -                     | -                 | -                        | SKS   | p       |
| FRS     | 96076 | 149              | 29                       | -85.            | 14.                   | 0.86              | 0.34                     | SKKS  | f       |
| FRS     | 95021 | 88               | 25                       | -82.            | -                     | -                 | -                        | SKS   | p       |
| FRS     | 95128 | 105              | 58                       | -57.            | -                     | -                 | -                        | SKS   | p       |
| FRS     | 95279 | 98               | 85                       | -74.            | -                     | -                 | -                        | SKS   | p       |
| FRS     | 95292 | 94               | 44                       | -23.            | -                     | -                 | -                        | SKS   | p       |
| FRS     | 95305 | 99               | 238                      | -27.            | -                     | -                 | -                        | SKS   | p       |
| FRS     | 95334 | 88               | 23                       | 79.             | -                     | -                 | -                        | SKS   | p       |
| MTH     | 95006 | 90               | 30                       | -77.            | -                     | -                 | -                        | SKS   | p       |
| MTH     | 95053 | 87               | 23                       | 16.             | -                     | -                 | -                        | SKS   | f       |
| MTH     | 95090 | 88               | 35                       | -74.            | 3.                    | 1.35              | 0.18                     | SKS   | f       |
| MTH     | 95111 | 105              | 58                       | -65.            | 9.                    | 1.60              | 0.35                     | SKS   | p       |
| MTH     | 95111 | 105              | 58                       | -71.            | 4.                    | 1.30              | 0.13                     | SKS   | f       |
| MTH     | 95113 | 104              | 58                       | -86.            | 6.                    | 1.15              | 0.18                     | SKS   | f       |
| MTH     | 95118 | 88               | 24                       | -52.            | -                     | -                 | -                        | SKS   | p       |
| MTH     | 95125 | 104              | 58                       | -78.            | 6.                    | 1.25              | 0.18                     | SKS   | g       |
| MTH     | 95128 | 105              | 58                       | -79.            | 4.                    | 1.35              | 0.13                     | SKS   | p       |
| MTH     | 95143 | 99               | 183                      | 14.             | -                     | -                 | -                        | SKS   | p       |
| MTH     | 95175 | 134              | 41                       | 88.             | 8.                    | 1.20              | 0.23                     | PKS   | g       |
| MTH     | 95175 | 134              | 41                       | -79.            | 8.                    | 1.50              | 0.33                     | SKKS  | p       |
| MTH     | 95181 | 89               | 43                       | -80.            | 4.                    | 2.40              | 0.30                     | SKS   | f       |
| MTH     | 95215 | 94               | 242                      | -74.            | 10.                   | 0.90              | 0.18                     | SKS   | f       |
| MTH     | 95226 | 133              | 44                       | -90.            | 9.                    | 1.10              | 0.20                     | PKS   | p       |
| MTH     | 95331 | 88               | 23                       | 19.             | -                     | -                 | -                        | SKS   | f       |
| MTH     | 95334 | 87               | 26                       | -81.            | -                     | -                 | -                        | SKS   | p       |
| MTH     | 95337 | 88               | 23                       | -64.            | -                     | -                 | -                        | SKS   | g       |
| MTH     | 96053 | 87               | 23                       | 16.             | -                     | -                 | -                        | SKS   | f       |
| MTH     | 96107 | 161              | 359                      | -74.            | -                     | -                 | -                        | SKKS  | p       |
| BSD     | 95006 | 90               | 29                       | -72.            | 3.                    | 1.85              | 0.43                     | SKS   | p       |
| BSD     | 95111 | 105              | 58                       | -63.            | 6.                    | 1.60              | 0.23                     | SKS   | f       |
| BSD     | 95113 | 105              | 58                       | -71.            | 13.                   | 1.20              | 0.25                     | SKKS  | f       |
| BSD     | 95118 | 88               | 24                       | 71.             | -                     | -                 | -                        | SKS   | f       |
| BSD     | 95175 | 134              | 41                       | 81.             | 8.                    | 0.65              | 0.13                     | PKS   | f       |
| BSD     | 95180 | 86               | 18                       | -66.            | -                     | -                 | -                        | SKS   | g       |
| BSD     | 95211 | 94               | 241                      | 83.             | -                     | -                 | -                        | SKKS  | f       |
| BSD     | 95215 | 94               | 242                      | -71.            | -                     | -                 | -                        | SKS   | g       |
| BSD     | 95215 | 94               | 242                      | -76.            | -                     | -                 | -                        | SKS   | p       |
| BSD     | 95231 | 78               | 266                      | 9.              | -                     | -                 | -                        | SKS   | f       |
| BSD     | 95235 | 110              | 37                       | -82.            | 10.                   | 0.70              | 0.15                     | SKS   | p       |
| BSD     | 95235 | 110              | 37                       | 75.             | 4.                    | 1.10              | 0.13                     | SKSdf | p       |
| BSD     | 95257 | 86               | 290                      | -81.            | -                     | -                 | -                        | SKS   | f       |
| BSD     | 95262 | 91               | 242                      | -88.            | 4.                    | 1.35              | 0.18                     | SKS   | p       |
| BSD     | 95291 | 95               | 44                       | -74.            | 12.                   | 1.45              | 0.45                     | SKS   | g       |
| BSD     | 95331 | 88               | 23                       | -70.            | -                     | -                 | -                        | SKS   | p       |
| BSD     | 95334 | 87               | 26                       | -81.            | -                     | -                 | -                        | SKS   | p       |
| BSD     | 95337 | 88               | 23                       | -79.            | -                     | -                 | -                        | SKS   | f       |
| BSD     | 95359 | 122              | 68                       | -77.            | 9.                    | 0.90              | 0.18                     | SKKS  | f       |
| BSD     | 96053 | 87               | 23                       | -81.            | -                     | -                 | -                        | SKS   | f       |
| BSD     | 96065 | 94               | 52                       | -79.            | 4.                    | 1.40              | 0.15                     | SKS   | f       |

**Table 3.** (continued)

| Station | Event | Distance,<br>deg | Back-<br>azimuth,<br>deg | $\phi$ ,<br>deg | $\sigma\phi$ ,<br>deg | $\delta t$ ,<br>s | $\sigma \delta t$ ,<br>s | Phase    | Quality |
|---------|-------|------------------|--------------------------|-----------------|-----------------------|-------------------|--------------------------|----------|---------|
| TRG     | 95006 | 90               | 29                       | -79.            | -                     | -                 | -                        | SKS      | p       |
| TRG     | 95107 | 88               | 21                       | 29.             | -                     | -                 | -                        | SKS      | f       |
| TRG     | 95111 | 105              | 57                       | -69.            | 3.                    | 1.90              | 0.15                     | SKS      | g       |
| TRG     | 95113 | 105              | 57                       | -71.            | 5.                    | 1.55              | 0.18                     | SKS      | g       |
| TRG     | 95122 | 84               | 260                      | -85.            | 9.                    | 1.25              | 0.38                     | SKS      | f       |
| TRG     | 95125 | 105              | 57                       | -78.            | 2.                    | 1.75              | 0.10                     | SKS      | f       |
| TRG     | 95128 | 106              | 57                       | -83.            | 6.                    | 1.75              | 0.28                     | SKS      | p       |
| TRG     | 95175 | 134              | 41                       | -77.            | 14.                   | 0.75              | 0.30                     | PKS      | f       |
| TRG     | 95175 | 134              | 41                       | -73.            | 3.                    | 1.65              | 0.15                     | SKKS     | f       |
| TRG     | 95180 | 86               | 18                       | 7.              | -                     | -                 | -                        | SKS      | f       |
| TRG     | 95181 | 89               | 302                      | 78.             | 15.                   | 0.95              | 0.30                     | SKS      | p       |
| TRG     | 95193 | 159              | 29                       | -88.            | 12.                   | 1.20              | 0.35                     | SKKS     | f       |
| TRG     | 95208 | 89               | 108                      | 26.             | -                     | -                 | -                        | SKKS     | f       |
| TRG     | 95215 | 93               | 242                      | 85.             | -                     | -                 | -                        | SKS      | f       |
| TRG     | 95231 | 78               | 265                      | 1.              | -                     | -                 | -                        | sSKS     | g       |
| TRG     | 95266 | 90               | 256                      | -81.            | 5.                    | 1.25              | 0.20                     | SKS      | g       |
| TRG     | 95291 | 95               | 44                       | -78.            | 4.                    | 1.70              | 0.23                     | SKS      | g       |
| TRG     | 95305 | 98               | 238                      | 71.             | 4.                    | 1.25              | 0.30                     | SKS      | f       |
| TRG     | 95337 | 89               | 23                       | -77.            | -                     | -                 | -                        | SKS      | g       |
| TRG     | 95359 | 122              | 68                       | -77.            | 10.                   | 0.70              | 0.17                     | SKKS     | f       |
| TRG     | 96053 | 88               | 23                       | -84.            | -                     | -                 | -                        | SKS      | f       |
| TRG     | 96065 | 94               | 52                       | -83.            | 6.                    | 1.45              | 0.18                     | SKS      | f       |
| TRG     | 96077 | 150              | 29                       | -83.            | 2.                    | 1.75              | 0.13                     | SKKS     | f       |
| TRG     | 96106 | 162              | 357                      | 9.              | -                     | -                 | -                        | SKS      | f       |
| VIL     | 95107 | 88               | 21                       | 69.             | 11.                   | 0.95              | 0.23                     | SKS      | f       |
| VIL     | 95111 | 105              | 57                       | -79.            | 8.                    | 1.00              | 0.15                     | SKS      | g       |
| VIL     | 95111 | 105              | 57                       | -84.            | 6.                    | 1.40              | 0.20                     | SKS      | f       |
| VIL     | 95113 | 105              | 57                       | -85.            | 8.                    | 1.50              | 0.30                     | SKS      | f       |
| VIL     | 95125 | 105              | 57                       | -86.            | 6.                    | 1.10              | 0.18                     | SKS      | g       |
| VIL     | 95128 | 106              | 57                       | -67.            | 20.                   | 0.75              | 0.38                     | SKS      | p       |
| VIL     | 95193 | 159              | 30                       | -83.            | 9.                    | 1.60              | 0.40                     | SKKS     | p       |
| VIL     | 95215 | 93               | 242                      | 79.             | 9.                    | 1.55              | 0.58                     | SKS      | p       |
| VIL     | 95226 | 134              | 45                       | 85.             | 9.                    | 0.80              | 0.23                     | PKS      | f       |
| VIL     | 95231 | 77               | 265                      | -85.            | -                     | -                 | -                        | sSKS     | f       |
| VIL     | 95257 | 86               | 289                      | 84.             | -                     | -                 | -                        | SKS      | p       |
| VIL     | 95266 | 103              | 86                       | -82.            | 4.                    | 1.30              | 0.35                     | SKS      | f       |
| VIL     | 95266 | 90               | 256                      | -64.            | 14.                   | 0.50              | 0.13                     | SKS      | f       |
| VIL     | 95279 | 98               | 85                       | -61.            | 21.                   | 0.50              | 0.35                     | SKS      | f       |
| VIL     | 95291 | 96               | 44                       | 79.             | 10.                   | 1.30              | 0.25                     | SKS      | g       |
| VIL     | 95292 | 95               | 44                       | 70.             | 7.                    | 2.5               | 0.40                     | SKS      | p       |
| VIL     | 95292 | 95               | 44                       | 75.             | 5.                    | 0.90              | 0.10                     | SKS      | f       |
| VIL     | 95305 | 98               | 238                      | 71.             | 6.                    | 1.25              | 0.38                     | SKS      | p       |
| VIL     | 95312 | 91               | 87                       | 16.             | -                     | -                 | -                        | SKS      | f       |
| VIL     | 95359 | 122              | 68                       | -82.            | 6.                    | 0.80              | 0.13                     | SKS      | g       |
| VIL     | 96065 | 94               | 52                       | 87.             | 7.                    | 1.20              | 0.23                     | SKS      | f       |
| VIL     | 96077 | 150              | 29                       | -86.            | 5.                    | 1.80              | 0.30                     | SKKS     | p       |
| VIL     | 96082 | 87               | 2                        | 18.             | -                     | -                 | -                        | SKS      | f       |
| VIL     | 96107 | 162              | 357                      | 3.              | -                     | -                 | -                        | SKKS     | f       |
| GRF     | 95107 | 89               | 21                       | 79.             | 5.                    | 2.15              | 0.30                     | SKS      | f       |
| GRF     | 95111 | 106              | 58                       | 83.             | 4.                    | 1.85              | 0.28                     | SKS      | g       |
| GRF     | 95113 | 106              | 58                       | 85.             | -                     | -                 | -                        | SKS      | p       |
| GRF     | 95118 | 90               | 24                       | -22.            | -                     | -                 | -                        | SKS      | p       |
| GRF     | 95125 | 105              | 58                       | -89.            | 3.                    | 1.40              | 0.10                     | SKS      | g       |
| GRF     | 95143 | 97               | 183                      | 78.             | -                     | -                 | -                        | SKS+SKKS | p       |
| GRF     | 95175 | 135              | 42                       | 75.             | 5.                    | 1.10              | 0.15                     | PKS      | f       |
| GRF     | 95180 | 156              | 30                       | 85.             | 4.                    | 2.15              | 0.13                     | SKKS     | p       |
| GRF     | 95180 | 87               | 18                       | 87.             | 4.                    | 1.75              | 0.30                     | SKS      | g       |
| GRF     | 95193 | 160              | 31                       | -84.            | 3.                    | 2.15              | 0.18                     | SKKS     | p       |
| GRF     | 95199 | 89               | 108                      | 88.             | -                     | -                 | -                        | SKS      | f       |
| GRF     | 95211 | 93               | 241                      | 72.             | -                     | -                 | -                        | SKS      | p       |
| GRF     | 95215 | 93               | 242                      | -85.            | 17.                   | 1.20              | 0.45                     | SKS      | f       |
| GRF     | 95226 | 135              | 45                       | 77.             | 7.                    | 1.40              | 0.23                     | PKS      | p       |
| GRF     | 95226 | 135              | 45                       | -67.            | -                     | -                 | -                        | SKS      | p       |
| GRF     | 95231 | 77               | 266                      | 79.             | -                     | -                 | -                        | SKS      | f       |
| GRF     | 95231 | 77               | 266                      | 4.              | -                     | -                 | -                        | sSKS     | g       |
| GRF     | 95266 | 90               | 256                      | -87.            | 6.                    | 1.15              | 0.25                     | SKS      | g       |

**Table 3.** (continued)

| Station | Event | Distance,<br>deg | Back-<br>azimuth,<br>deg | $\phi$ ,<br>deg | $\sigma\phi$ ,<br>deg | $\delta t$ ,<br>s | $\sigma\delta t$ ,<br>s | Phase    | Quality |
|---------|-------|------------------|--------------------------|-----------------|-----------------------|-------------------|-------------------------|----------|---------|
| GRF     | 95291 | 97               | 44                       | -83.            | 8.                    | 1.90              | 0.40                    | SKS+SKKS | f       |
| GRF     | 95305 | 97               | 238                      | 88.             | 7.                    | 1.70              | 0.30                    | SKS      | f       |
| GRF     | 95337 | 90               | 22                       | 84.             | 3.                    | 2.00              | 0.23                    | SKS      | f       |
| GRF     | 96001 | 111              | 70                       | 77.             | -                     | -                 | -                       | SKS      | g       |
| GRF     | 96038 | 89               | 22                       | 69.             | -                     | -                 | -                       | SKS      | p       |
| GRF     | 96077 | 151              | 29                       | 84.             | 3.                    | 2.30              | 0.10                    | SKKS     | p       |
| GRF     | 96090 | 87               | 354                      | -86.            | -                     | -                 | -                       | SKS      | f       |
| GRF     | 96107 | 163              | 356                      | -82.            | -                     | -                 | -                       | SKKS     | p       |
| ORG     | 95036 | 175              | 24                       | 8.              | -                     | -                 | -                       | SKKS     | p       |
| ORG     | 95107 | 88               | 21                       | -83.            | 5.                    | 1.50              | 0.40                    | SKS      | f       |
| ORG     | 95118 | 89               | 23                       | -78.            | -                     | -                 | -                       | SKS      | f       |
| ORG     | 95291 | 96               | 44                       | -61.            | 11.                   | 1.25              | 0.46                    | SKS      | p       |
| ORG     | 95304 | 98               | 46                       | -77.            | 7.                    | 0.80              | 0.10                    | SKS      | f       |
| ORG     | 95336 | 89               | 22                       | 32.             | -                     | -                 | -                       | SKS      | f       |
| ORG     | 95337 | 89               | 22                       | -58.            | -                     | -                 | -                       | SKS      | f       |
| ORG     | 96038 | 88               | 22                       | 32.             | -                     | -                 | -                       | SKS      | f       |
| ORG     | 96065 | 94               | 52                       | -63.            | -                     | -                 | -                       | SKS      | p       |
| BRU     | 95036 | 175              | 30                       | 68.             | 16.                   | 0.95              | 0.28                    | SKKS     | f       |
| BRU     | 95111 | 105              | 58                       | -80.            | 10.                   | 0.90              | 0.18                    | SKS      | g       |
| BRU     | 95111 | 105              | 58                       | -82.            | 3.                    | 0.95              | 0.08                    | SKS      | g       |
| FNM     | 95111 | 105              | 58                       | -60.            | 5.                    | 1.25              | 0.18                    | SKS      | g       |
| ALB     | 95111 | 105              | 58                       | -66.            | 3.                    | 2.20              | 0.15                    | SKS      | f       |
| ALB     | 95257 | 87               | 290                      | -81.            | -                     | -                 | -                       | SKS      | f       |
| ALB     | 95266 | 102              | 87                       | -60.            | 11.                   | 1.9               | 0.29                    | SKKS     | p       |
| ALB     | 95266 | 102              | 87                       | 89.             | 6.                    | 1.54              | 0.48                    | SKS      | g       |
| ALB     | 95279 | 98               | 86                       | -68.            | 10.                   | 1.06              | 0.27                    | SKKS     | f       |
| ALB     | 95291 | 95               | 45                       | -69.            | 2.                    | 2.34              | 0.18                    | SKS      | g       |
| ALB     | 95305 | 98               | 239                      | 79.             | 3.                    | 1.25              | 0.16                    | SKS      | g       |
| ALB     | 95336 | 89               | 23                       | 89.             | -                     | -                 | -                       | SKS      | f       |
| ALB     | 95337 | 89               | 23                       | -83.            | -                     | -                 | -                       | SKS      | p       |
| ALB     | 96053 | 88               | 23                       | -75.            | -                     | -                 | -                       | SKS      | f       |
| LAR     | 96198 | 112              | 67                       | -65.            | -                     | -                 | -                       | SKS+SKKS | p       |
| LAR     | 96204 | 112              | 67                       | 87.             | -                     | -                 | -                       | SKS+SKKS | p       |
| LAR     | 96249 | 97               | 52                       | -60.            | 3.                    | 1.10              | 0.15                    | SKS      | g       |
| LAR     | 96255 | 94               | 30                       | -69.            | -                     | -                 | -                       | SKS      | p       |
| LAR     | 96293 | 94               | 39                       | -74.            | 7.                    | 1.35              | 0.25                    | SKS      | g       |
| LAR     | 96310 | 168              | 356                      | -63.            | 4.                    | 1.90              | 0.25                    | SKKS     | p       |
| AUS     | 96357 | 87               | 28                       | -80.            | 2.                    | 1.20              | 0.13                    | SKS      | g       |
| AUS     | 97023 | 88               | 237                      | -60.            | 2.                    | 1.30              | 0.08                    | SKS      | g       |
| AUS     | 97084 | 82               | 250                      | -74.            | 10.                   | 1.25              | 0.95                    | S(609km) | f       |
| RVH     | 96249 | 96               | 52                       | 40.             | -                     | -                 | -                       | SKKS     | p       |
| RVH     | 96293 | 93               | 39                       | -70.            | -                     | -                 | -                       | SKS      | g       |
| RVH     | 96357 | 87               | 28                       | -70.            | 2.                    | 1.45              | 0.23                    | SKS      | g       |
| RVH     | 97149 | 121              | 249                      | -64.            | -                     | -                 | -                       | SKS      | p       |
| PYO     | 96293 | 93               | 39                       | -68.            | 5.                    | 1.45              | 0.28                    | SKS      | g       |
| PYO     | 96357 | 86               | 28                       | -84.            | -                     | -                 | -                       | SKS      | p       |
| PYO     | 97145 | 168              | 358                      | 4.              | -                     | -                 | -                       | SKKS     | p       |
| LEI     | 96357 | 87               | 28                       | -73.            | 2.                    | 1.50              | 0.20                    | SKS      | g       |
| LEI     | 97023 | 87               | 237                      | -78.            | 1.                    | 1.45              | 0.05                    | SKS      | g       |
| RON     | 96357 | 87               | 28                       | -84.            | 4.                    | 1.65              | 0.23                    | SKS      | g       |
| RON     | 97145 | 169              | 357                      | -84.            | -                     | -                 | -                       | SKS      | f       |
| RON     | 97145 | 169              | 357                      | -72.            | 4.                    | 1.30              | 0.15                    | SKKS     | g       |

The shear phase is indicated together with a quality of the measurements (g, good; f, fair; p, poor). For "null" results (events for which no signal has been found on the transverse component) only the distance and backazimuth are reported.

central Pyrenees. Their observations revealed a highly conductive body beneath the Pyrenean Axial Zone down to 80 km depth, which contrasts with a highly resistive upper mantle farther north. They interpret this anomaly as subducted crustal material, with possible partial melt beneath the PAZ. Some interesting features appear combining our shear wave splitting observations with upper mantle seismic tomography results (Figure 5a). In the central and eastern Pyrenees, large  $\delta t$  are observed at stations located above the low-velocity anomaly in the upper mantle, whereas smaller values are observed at the periphery. This could suggest that dipping lithospheric material, for which the crustal part only is visible in tomographic maps, is responsible for the large splitting. However, in western Pyrenees, where no subduction took place, large  $\delta t$  values are also observed. Thus another explanation has to be found. The splitting parameter pattern, however, confirms the departure from cylindrical symmetry previously observed from other geophysical data.

An E-W elongated negative Bouguer gravity anomaly [Casas *et al.*, 1997; De Cabissole, 1989; Grandjean, 1994; Torne *et al.*, 1989] beneath the Axial and South Pyrenean Zone (Figure 5b) is consistent with an abnormally thick Iberian crust. High positive Bouguer anomalies in the North Pyrenean Zone are likely related to a thinner Eurasian crust and to mantle intrusions within the crust along the belt; some of the latter are observed in crustal seismic tomography studies [Grandjean, 1994; Souriau and Granet, 1995]. Combining anisotropy information together with the Bouguer anomaly map (Figure 5b) does not reveal any significant correlation, indicating that the source of anisotropy is located beneath the source of this gravimetric anomaly, i.e., at subcrustal levels. This is true even for stations located at the two prominent gravity anomalies ("Saint Gaudens" and "Labourd" anomalies) in the western and central Pyrenees, which are interpreted as due to the presence of an upper mantle body at crustal depth [Grandjean, 1994; Torne *et al.*, 1989].

## 5. Tectonic Origin of Anisotropy

The tectonic evolution of the Pyrenean domain was long lasting and continues today. Several deformation episodes may have contributed to the lithospheric fabric responsible for seismic anisotropy. Possible origins of anisotropy are discussed from present-day to past tectonic processes: today's state of stress, pervasive deformation related to the Pyrenean orogeny and pre-Pyrenean pervasive structures.

### 5.1. Stress-Induced Anisotropy and Crustal Contribution to Shear Wave Splitting

Microcrack-induced anisotropy [Crampin, 1984] may explain delay times of a few tenths of seconds and is generally correlated to the state of stress in the upper crust. The present-day state of stress in the Pyrenees is characterized by rather complex pattern. The world stress map [Zoback, 1992] shows maximum horizontal stress directions in the western Pyrenees varying from NW-SE to NE-SW over short distances. Regional earthquake focal mechanisms [Delouis *et al.*, 1993; Rigo *et al.*, 1997] indicate a complex stress field in the Pyrenees. Interpolation of the stress data in France provided by Rebai *et al.* [1992] seems however to indicate a maximum horizontal compressive direction oriented roughly N-S in the eastern and central Pyrenees and NW-SE in the western Pyrenees. Assuming a stress-controlled anisotropy, the fast split shear waves should parallel open microcracks and

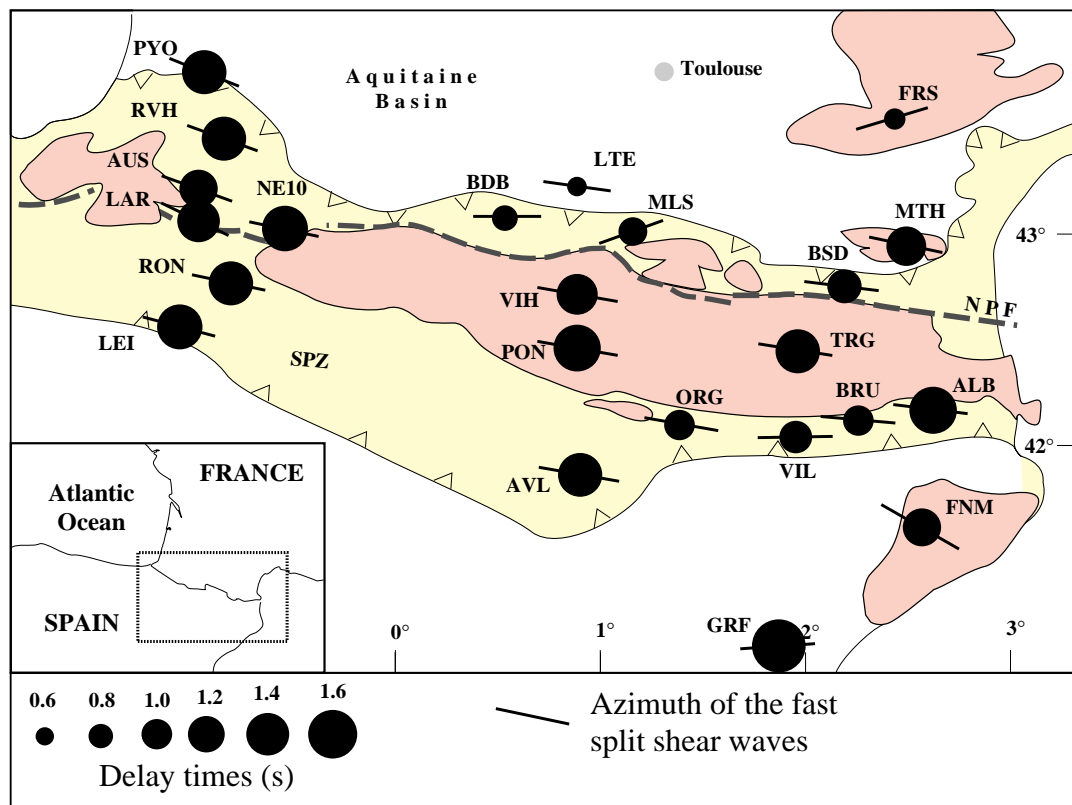


**Figure 4.** Map of the SKS splitting results in the Pyrenees from this study (in the eastern and western Pyrenees), from Barruol and Souriau [1995] in the central Pyrenees, and from Souriau and Njike-Kassala [1993] for the NARS station NE10. For each station, the mean value deduced from individual splitting measurements is represented by a circle whose radius is proportional to  $\delta t$ ; the solid segment represents the azimuth of the fast direction  $\phi$ .

therefore the trend of maximum compression direction, a situation which is clearly not observed. From the lack of correlation of the anisotropy with present-day stress field in the Pyrenees, we conclude that microcracks-induced anisotropy in the upper crust does not dominate the observed shear wave splitting. The N-S direction of compression observed in the crust reflects the present-day convergence of the plates. At upper mantle level, this compression may currently produce an E-W trending fabric, compatible with our measurements. We discuss these possible processes in section 5.3.

Lower crustal shear wave splitting is difficult to detect, but several studies [e.g., Herquel *et al.*, 1995; McNamara and Owens, 1993] indicate that 0.1 to 0.3 s delay times could be attributed to pervasive lower crustal fabric. These observations are in agreement with petrophysical predictions based on typical crustal fabrics that lead to delay times of around 0.1 s per 10 km thickness of anisotropic medium [Barruol and Mainprice, 1993]. In summary, the crust likely contributes to the total splitting (up to 10 to 20% of the observed delays) but cannot alone explain our observations (delay times higher than 1 s and often around 1.5 s).

## 5.2. Paleogene and Neogene Deformations in the Catalan Coastal Ranges

The Miocene opening of the western Mediterranean basin (21 Ma) was preceded by Oligocene extensional tectonics (25 Ma) along the northeastern part of the Iberian continental margin where two of our stations (FNM and GRF) are located. This extension created the Valencia trough, southeast of Barcelona [Banda and Santanach, 1992] and induced the uplift of the rift's

shoulder and the formation of the Catalan coastal ranges (Figure 1). The related crustal thinning is well imaged by seismic reflection profiling of the Iberian margin [e.g., Gallart *et al.*, 1994] that shows a crustal thickness reduced from 30 to 15 km over a few tenths of a kilometer offshore. Crustal extensional structures exposed in the Catalan coastal ranges are NE-SW trending grabens associated to NW-SE transcurrent faults [Vegas, 1992]. Although crustal thinning related to the Valencia trough opening seems to be restricted offshore, the Miocene paleostress directions as deduced from brittle structures onshore are consistent with an EW to NW-SE direction of extension [Bartrina *et al.*, 1992].

Assuming coherent deformation of the lithosphere, the upper mantle stretching related to this tectonic episode beneath the Catalan coastal ranges should result in a shallow to moderately dipping foliation and in an E-W to NW-SE trending flow direction (lineation). The corresponding anisotropy should trend parallel to the flow direction. Our observations at FNM ( $\phi = N120^\circ$  but deduced from a single measurement) and at GRF ( $\phi = N86^\circ$ ) may be compatible with such a trend. However, upper mantle xenolith seismic properties are such that a flat-lying foliation is weakly anisotropic ( $< 2\%$ ) for a vertically propagating shear wave [Ji *et al.*, 1994; Mainprice and Silver, 1993]. The strong anisotropy recorded at GRF ( $\delta t = 1.75$  s) is therefore hardly compatible with this explanation alone. A Miocene anisotropy may be superimposed on the Hercynian fabrics at the base of the lithosphere on the eastern edge of the Pyrenees but two anisotropies of different ages with similar orientations cannot be distinguished by the method. However, the homogeneity of the

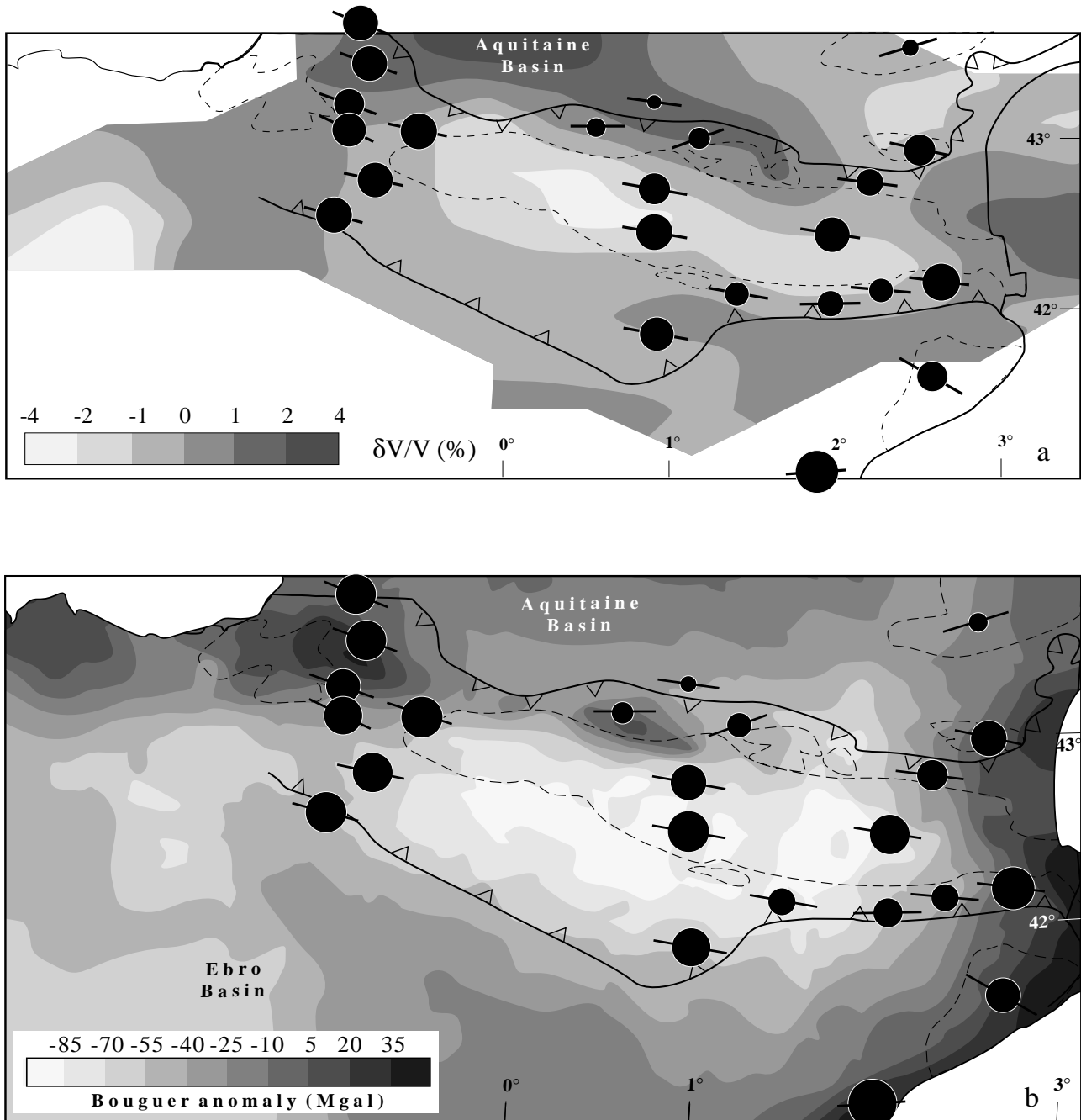


**Figure 5.** Map of SKS splitting results in the Pyrenees superimposed on (a)  $P$  wave velocity heterogeneity at depth of 50 to 100 km from *Souriau and Granet* [1995]. The low-velocity body beneath the axial zone is interpreted as Iberian lower crust subduction. (b) Bouguer anomaly adapted from *Grandjean* [1992] and *De Cabissole* [1989]. Note the low and broad anomaly parallel to the trend of the belt corresponding to the Iberian crust thickening toward the north and the high anomalies in the NPZ corresponding likely to upper mantle bodies at crustal depth.

results obtained in the eastern Pyrenees with those obtained from the central and western profiles suggests that extension-related fabric does not dominate the signal.

### 5.3. Pyrenean Anisotropy

The Pyrenean orogeny can be divided into two distinct phases: (1) rotation of Iberia with respect to Eurasia during Albian-Cenomanian times (100 Ma) that resulted in a large left-lateral

strike-slip motion and in the thinning of the Eurasian margin. Related to this tectonic episode is a mantle upwelling responsible for both emplacement of the upper mantle slices in the shallow crust [*Vielzeuf and Kornprobst*, 1984] and high-temperature metamorphism [*Golberg and Leyreloup*, 1990] affecting the rift sediments (the present-day North Pyrenean Zone); (2) N-S collision that began at late Cretaceous (about 80 Ma) but culminated during Eocene times, about 45 Ma [e.g., *Choukroune*, 1992]. From the plate reconstruction [*Choukroune*, 1992; *Olivet*,

1996], the total strike-slip displacement is estimated around 200–300 km, and the proposed N-S shortening during the collision between the two plates is probably around 100 km. Figure 6 shows a possible interpretation of the origin of the anisotropy through successive cartoons from late Hercynian event to present-day situation.

During the Albian-Cenomanian strike-slip motion of the plates, the lithosphere is extremely thinned, and the flow direction in the asthenospheric mantle wedge beneath the rifted domain is expected to be roughly parallel to the rift direction (Figure 6b). The narrowness (less than 20 km) of the domain affected by crustal deformation and high-temperature metamorphism suggests that the upper mantle rifted zone is narrow too. Taking into account upper mantle seismic properties determined from xenolith studies [Ben Ismail and Mainprice, 1998; Ji et al., 1994; Mainprice and Silver, 1993], the related anisotropy at that stage is

expected to be characterized by a  $\phi$  trending parallel to the trend of the belt.

The N-S Eocene collision resulted in crustal shortening accommodated by thrusts and nappes and incipient crustal subduction. Considering that this collision involved an extremely thinned lithosphere, the N-S closure of this domain may have resulted in E-W flow of the asthenospheric mantle beneath the North Pyrenean Zone but also in a high-temperature deformation of the two lithospheric walls (Figure 6c). A similar process of lateral mantle flow has been previously proposed by Russo and Silver [1994] to explain splitting measurements in western South America. In the Pyrenees, such deformation should result in E-W preferred orientation of olivine  $a$  axis, similar to the fabrics expected during the previous strike-slip episode. We note that the lateral anisotropy variations along the North Pyrenean Zone are consistent with the hypothesis of material extrusion in front of the

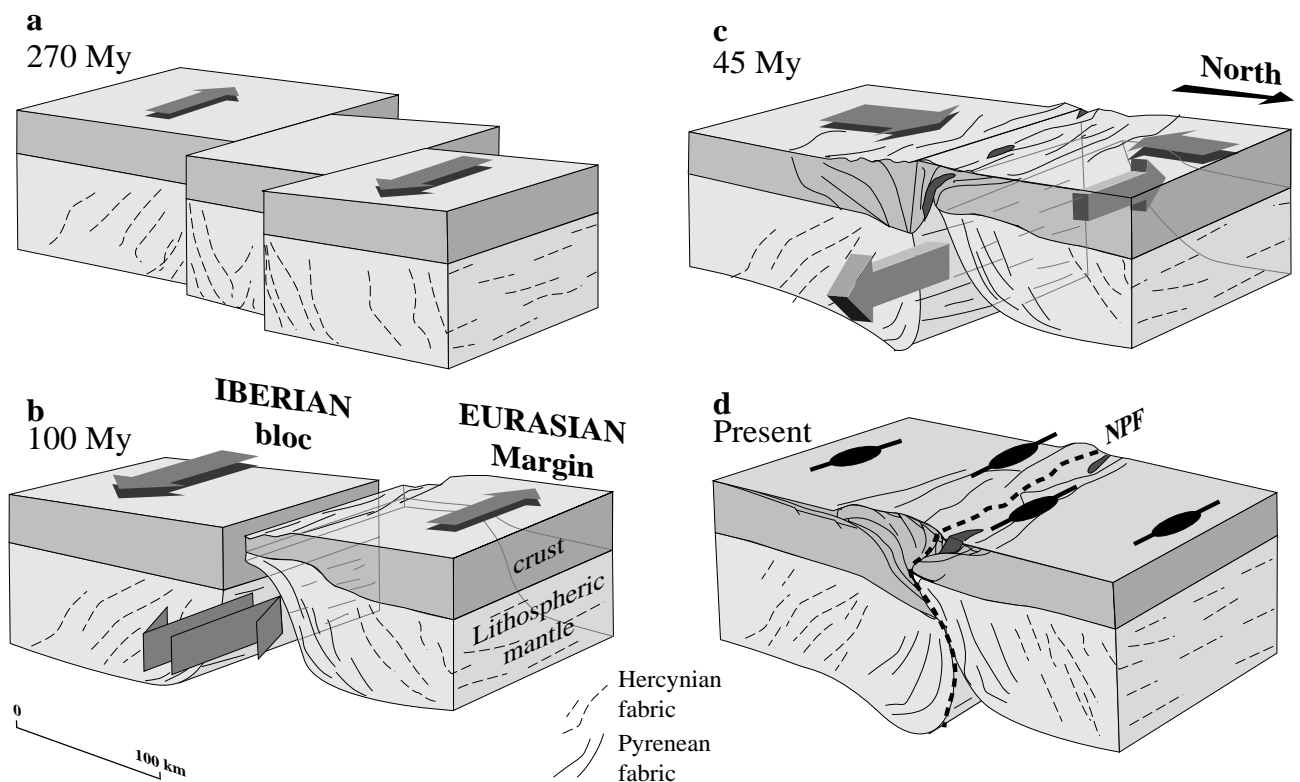


**Figure 6.** Schematic lithospheric-scale blocs diagrams illustrating the evolution of the Pyrenees since late Hercynian times. (a) At the end of the Variscan orogeny (270 Ma), a large-scale dextral strike-slip fault occurs at the future place of the Pyrenean belt, generating a strong pervasive deformation of the upper mantle. (b) During Albian times (about 100 Ma), the rotation of the Iberian bloc with respect to the Eurasian plate, induced by the North Atlantic and the bay of Biscaye opening, created a long and narrow rift on a sinistral transcurrent zone (the present-day North Pyrenean Zone). This episode is accompanied by asthenospheric upwelling, lherzolite emplacement at very shallow depth, and high-temperature metamorphism of the rift sediments. We propose that both the asthenospheric wedge beneath the rift and the neighboring lithospheres may be pervasively deformed at that stage, with an E-W trending lineation. (c) As proposed by Mattauer [1990], at upper Cretaceous (around 80 Ma) the N-S motion of the Iberian bloc began, inducing the closure of the E-W trending rift. We suggest that the hot upper mantle between the two lithospheric blocs may have been laterally extruded. E-W trending lineations could result from this deformation in both the asthenosphere and deep lithosphere. (d) The present-day upper mantle structures beneath the belt could correspond to steeply dipping foliations and E-W trending lineations, acquired either during the Pyrenean built-up (since 100 Ma) for the central part of the belt or during the late Hercynian tectonic episodes for the external parts of the belt. Part of the observed anisotropy may result from present-day upper mantle flow related to the convergence between the two lithospheres. The Hercynian upper mantle pervasive deformation is schematized by dashed lines and the Pyrenean (active or frozen) fabric by continuous lines.

northward moving Iberian plate;  $\delta t$  is much smaller in the central part of the belt (LTE, MLS, BDB) than on the eastern (MTH and BSD) and western edges (PYO and RVH), where the mantle flow is expected to be maximum. That may represent a stagnation point where the strain is expected to be small or null [Russo and Silver, 1994].

The closure and the cooling of the system likely resulted at present day in a complex upper mantle structure beneath the central part of the belt, derived from high-temperature mantle deformation, either in the deep lithosphere or in the asthenosphere trapped between the two lithospheric blocs during collision (Figure 6d). Part of this hot mantle may have been incorporated into the lithosphere by cooling and part may remain beneath the NPZ. Although the present-day deformation of the Pyrenees is small, it may be accommodated by upper mantle flow. Therefore part of the recorded anisotropy may be related to active upper mantle deformation beneath the belt. Since the deformation regime of the Pyrenees did not change significantly since Eocene times, a possible anisotropy generated by present-day mantle flow beneath the Pyrenees cannot be distinguished from the previously developed fabric.

In summary, stations located in the Pyrenean Axial Zone (TRG, VIH, PON, LAR, and AUS) and in the North Pyrenean Zone (BSD, MLS, BDB, PYO, and RVH) may therefore likely record a "true" Pyrenean anisotropy, that is, an anisotropy related to either frozen or active Pyrenean tectonics.

#### 5.4. Hercynian Anisotropy

Farther south (at GRF, AVL, RON, for instance), it is unlikely that the Pyrenean orogeny reactivated the whole upper mantle fabric (see discussion of Vauchez and Barruol [1996]). A pre-Pyrenean origin of anisotropy is likely for these stations. As suggested by Arthaud and Matte [1977] and more recently by Gleizes *et al.* [1997], the whole Pyrenean belt was involved in a broad zone of dextral strike slip motion during the late stage of the Variscan orogen (Figure 6a). Field observations reveal the presence of an E-W trending zone of transpression, characterized by steeply dipping foliations, particularly in the eastern and central Pyrenees [Carreras and Cirès, 1986; Soliva, 1992]. Such a strike-slip regime of deformation is particularly efficient at generating large magnitude of anisotropy; first, because it may coherently deform the whole lithosphere and, second, because it creates steeply dipping foliations and horizontal lineations, a structural fabric that appears as the most anisotropic for a vertically propagating shear wave, both in the crust [Barruol and Mainprize, 1993] and in the upper mantle [Mainprize and Silver, 1993].

At FRS in the southern Massif Central, although  $\phi$  is roughly parallel to the Eurasian plate motion vector, it is also consistent with the Hercynian fabric. The axial zone of the "Montagne Noire" (see Figure 1) is composed of a gneissic dome elongated N070°E, parallel to a late Hercynian dextral strike slip fault [Bard, 1997; Nicolas *et al.*, 1977]. The observed fast direction is parallel to the trend of the Hercynian crustal structure and may be compatible with frozen lithospheric deformation. However, the complex pattern of nulls obtained at this site suggests the presence of a complex structure beneath this site, such as dipping symmetry axis of anisotropy or several anisotropic layers. The asthenospheric mantle plume imaged by seismic tomography beneath the Massif Central [Granet *et al.*, 1995] can provide such an explanation.

Whether the anisotropy recorded in the Pyrenean Axial Zone (stations VIH and PON in the central Pyrenees, TRG in the eastern

Pyrenees, and perhaps ORG, VIL, BRU, and ALB which are very close to its southern boundary; stations NE10, LAR, and RON in the western Pyrenees) is produced by Pyrenean or Hercynian frozen structures remain uncertain. These stations are close to the North Pyrenean Zone, and therefore their anisotropy may reflect the Pyrenean orogeny. The low-velocity strip beneath the Pyrenean Axial Zone (Figure 5a) suggests the presence of low velocity material down to 50-100 km depth. If this low-velocity corresponds to crustal material, part of the total splitting at these stations may reflect deep crustal Pyrenean deformation. On the other hand, if this low-velocity zone corresponds to partial melting, as suggested by Pous *et al.* [1995], part of the splitting may reflect the orientation of the melt films or pockets at depth. However, since the two deformations (Hercynian and Pyrenean) are expected to give similar anisotropy signatures, both effects may be present and cannot be distinguished by shear wave splitting analysis.

## 6. Conclusions

The three profiles along which teleseismic shear wave splitting is measured give a rather comprehensive view of upper mantle seismic anisotropy beneath the Pyrenean belt. At this scale, seismic anisotropy appears very homogeneous from both the fast split wave polarization direction (N100° to N110°E) and the amplitude of the observed delay times  $\delta t$  (generally above 1 s and often in the range 1.3 to 1.5 s). This clearly points out the existence of a rather large intrinsic anisotropy in the upper mantle.

From (1) the poor correlation of the observed anisotropy with the present-day plate motion, (2) the short-scale variation of the splitting parameters, (3) the parallelism of the fast wave polarization direction with the outcropping crustal structures, and (4) the good fit between the SKS anisotropy and the  $P_n$  anisotropy, we suggest that most of the anisotropy is located within the uppermost mantle, either frozen in the lithosphere or related to present-day upper mantle deformation beneath the central part of the belt. These structures may be related either to the Pyrenean or to the Hercynian orogeny.

We suggest that the stations located outside and on the external units of the belt record an anisotropy due to a regional-scale transcurrent Hercynian deformation. On the other hand, stations located on the North Pyrenean Zone and perhaps on the Axial Zone of the Pyrenees, the two units most affected by the Pyrenean tectonics, are compatible with upper mantle deformation due to the Pyrenean orogeny. The first episode of this orogeny is a sinistral strike-slip motion of Iberia relative to Eurasia that occurred during Albian times, 100 Ma, and generated elongated rift zones, associated with asthenospheric mantle upwelling. The second episode that may have affected the upper mantle structure is the N-S collision between the two plates that took place mainly during Eocene times, about 45 Ma. We propose that lateral mantle extrusion during the N-S closure of the rift may explain the large E-W anisotropy observed along the belt. Since the convergence regime did not change significantly since Eocene times, part of the anisotropy recorded in the central part of the belt may reflect an active upper mantle flow related to present-day tectonics.

No particularly large variation in anisotropy is correlated with the North Pyrenean Fault. This fault represents the former boundary between the Iberian and the Eurasian plates, along which the relative plate motions could have induced a local

increase of deformation and anisotropy. This is not the case: The deformation along this fault is either too narrow at depth to be visible by the technique we use, or it is not stronger than the neighboring pervasive Pyrenean deformation.

**Acknowledgments.** This project is a contribution to the program Imagerie et Dynamique de la Lithosphère (IDYL) supported by the CNRS/INSU. Many thanks to all the people that helped us during the field surveys, particularly R. Russo, W. Ben Ismail, A. Tommasi, E. Ferreira, F. Samarcq, M. Sylvander, M. Vadell, A. Rigo, J.M. Douchain, and also to J. F. Fels for his help in data processing. We are grateful to P. Silver for allowing us to use his splitting analysis program. We also thank the mayors and farmers of several villages for their help in providing site installations, in particular, at La Salvetat sur Agout, Bessède de Sault, Aussurucq, and Ramous-Puyoo. We are also indebted to the Catalan Seismic Survey which allowed us to set up some stations on their sites. J.T. and J.C. acknowledge support from project UPV001.310-EB003/95. The comments and suggestions of K. Fischer, J. Ni, and R. Russo contributed significantly to the final version of this paper.

## References

- Arthaud, F., and P. Matte, Late Paleozoic strike-slip faulting in southern Europe and northern Africa: Result of a right-lateral shear zone between the Appalachians and the Urals, *Geol. Soc. Am. Bull.*, **88**, 1305-1320, 1977.
- Banda, E., and P. Santanach, The Valencia trough (western Mediterranean): An overview, *Tectonophysics*, **208**, 183-202, 1992.
- Bard, J.P., Démembrement anté-Mésozoïque de la chaîne varisque d'Europe occidentale et d'Afrique du Nord: Rôle essentiel des grands décrochements transpressifs dextres accompagnant la rotation-translation horaire de l'Afrique durant le Stéphanien, *C. R. Acad. Sci., Ser. 2*, **324**, 693-704, 1997.
- Barruol, G., and D. Mainprice, A quantitative evaluation of the contribution of crustal rocks to the shear wave splitting of teleseismic SKS waves, *Phys. Earth Planet. Inter.*, **78**, 281-300, 1993.
- Barruol, G., and A. Souriau, Anisotropy beneath the Pyrenees range from teleseismic shear wave splitting, *Geophys. Res. Lett.*, **22**, 493-496, 1995.
- Bartrina, M.T., L. Cabrera, M.J. Jurado, J. Guimera, and E. Roca, Evolution of the central Catalan margin of the Valencia trough (western Mediterranean), *Tectonophysics*, **203**, 219-247, 1992.
- Ben Ismail, W., and D. Mainprice, An olivine fabric database: An overview of upper mantle fabrics and seismic anisotropy, *Tectonophysics*, in press, 1998.
- Bormann, P., G. Gruenthal, R. Kind, and H. Montag, Upper mantle anisotropy underneath central Europe: Effect of absolute plate motion and lithosphere-asthenosphere boundary topography?, *J. Geodyn.*, **22**, 11-32, 1996.
- Carreras, J., and J. Cirès, The geological significance of the western termination of the Mérens fault at Port Vell (Central Pyrenees), *Tectonophysics*, **129**, 99-114, 1986.
- Casas, A., P. Kearey, L. Rivero, and C.R. Adam, Gravity anomaly map of the Pyrenean region and a comparison of the deep geological structure of the western and eastern Pyrenees, *Earth Planet. Sci. Lett.*, **150**, 65-78, 1997.
- Choukroune, P., Tectonic evolution of the Pyrenees, *Annu. Rev. Earth Planet. Sci.*, **20**, 143-158, 1992.
- Crampin, S., Effective anisotropic elastic constants for wave propagation through cracked solids, *Geophys. J. R. Astron. Soc.*, **76**, 135-145, 1984.
- Daignières, M., J. Gallart, E. Banda, and A. Hirn, Implication of the seismic structure for the orogenic evolution of the Pyrenees range, *Earth Planet. Sci. Lett.*, **57**, 88-110, 1982.
- De Cabissole, B., Apport des données gravimétriques à la connaissance de la chaîne des Pyrénées le long du profil ECORS, doctorat thesis, Univ. de Montpellier II, Montpellier, France, 1989.
- Delouis, B., H. Haessler, A. Cisternas, and L. Rivera, Stress tensor determination in France and neighbouring regions, *Tectonophysics*, **221**, 413-437, 1993.
- DeMets, C., R.G. Gordon, D.F. Argus, and S. Stein, Current plate motions, *Geophys. J. Int.*, **101**, 425-478, 1990.
- Gallart, J., N. Vidal, J.J. Danobeitia, and ESCI Group, Lateral variations in the deep structure at the Iberian margin of the Valencia trough imaged from seismic reflection methods, *Tectonophysics*, **232**, 59-75, 1994.
- Gleizes, G., D. Leblanc, and J.L. Bouchez, Variscan granites of the Pyrenees revisited: Their role as syntectonic markers of the orogen, *Terra Nova*, **9**, 38-41, 1997.
- Golberg, J.M., and A.F. Leyreloup, High temperature-low pressure Cretaceous metamorphism related to crustal thinning (eastern North Pyrenean Zone, France), *Contrib. Mineral. Petrol.*, **104**, 194-207, 1990.
- Grandjean, G., Mise en évidence des structures crustales dans une portion de chaîne et de leur relation avec les bassins sédimentaires. Application aux Pyrénées occidentales au travers du projet ECORS Arzacq-Pyrénées, doctorat thesis, Univ. de Montpellier II, Montpellier, France, 1992.
- Grandjean, G., Etude des structures crustales dans une portion de chaîne et de leur relation avec les bassins sédimentaires. Application aux Pyrénées occidentales, *Bull. Cent. Rech. Explor. Prod. Elf Aquitaine*, **18**, 391-420, 1994.
- Granet, M., G. Stoll, J. Dorel, U. Achauer, G. Poupinet, and K. Fuchs, Massif Central (France): New constraints on the geodynamical evolution from teleseismic tomography, *Geophys. J. Int.*, **121**, 33-48, 1995.
- Granet, M., U. Achauer, and S. Judenherc, Using anisotropic Pn tomography and SKS-wave splitting analysis to investigate the geotectonic setting of upper mantle structures beneath France, *Terra Nova*, **9**, p. 75, EUG, Strasbourg, France, 1997.
- Gripp, A.E., and R.G. Gordon, Current plate velocities relative to the hotspots incorporating the Nuvel-1 global plate motion model, *Geophys. Res. Lett.*, **17**, 1109-1112, 1990.
- Herquel, G., G. Wittlinger, and J. Guilbert, Anisotropy and crustal thickness of northern Tibet: New constraints for tectonic models, *Geophys. Res. Lett.*, **22**, 1925-1928, 1995.
- Ji, S., X. Zhao, and D. Francis, Calibration of shear-wave splitting in the subcontinental upper mantle beneath active orogenic belts using ultramafic xenoliths from the Canadian cordillera and Alaska, *Tectonophysics*, **239**, 1-27, 1994.
- Kennett, B.L.N., Seismic traveltime tables, in *Global Earth Physics: A Handbook of Physical Constants*, AGU Ref. Shelf, vol 1, edited by T.J. Ahrens, pp. 126-143, AGU, Washington, D. C., 1995.
- Mainprice, D., and P.G. Silver, Interpretation of SKS-waves using samples from the subcontinental lithosphere, *Phys. Earth Planet. Inter.*, **78**, 257-280, 1993.
- Marson-Pidgeon, M., and M.K. Savage, Frequency-dependent anisotropy in Wellington, New Zealand, *Geophys. Res. Lett.*, **24**, 3297-3300, 1997.
- Mattauer, M., Une autre interprétation du profil ECORS Pyrénées, *Bull. Soc. Géol. Fr.*, **VI**, (8), 307-311, 1990.
- McNamara, D.E., and T.J. Owens, Azimuthal shear wave velocity anisotropy in the Basin and Range province using Moho Ps converted phases, *J. Geophys. Res.*, **98**, 12003-12017, 1993.
- Nicolas, A., and N.I. Christensen, Formation of anisotropy in upper mantle peridotites-A review, in *Composition, Structure and Dynamics of the Lithosphere-Asthenosphere System*, Geodyn. Ser., vol. 16, edited by K. Fuchs, and C. Froidevaux, pp. 111-123, AGU, Washington, D.C., 1987.
- Nicolas, A., J.L. Bouchez, J. Blaise, and J.P. Poirier, Geological aspects of deformation in continental shear zones., *Tectonophysics*, **42**, 55-73, 1977.
- Olivet, J.L., Kinematics of the Iberian plate, *Bull. Cent. Rech. Explor. Prod. Elf Aquitaine*, **20**, 131-195, 1996.
- Poupinet, G., A. Souriau, M. Vadell, and J.D. Njike-Kassala, Constraints on the lithospheric structure beneath the North Pyrenean Fault from teleseismic observations, *Geology*, **20**, 157-160, 1992.
- Pous, J., J. Ledo, A. Marcuello, and M. Daignières, Electrical resistivity model of the crust and upper mantle from magnetotelluric survey through the central Pyrenees, *Geophys. J. Int.*, **121**, 750-762, 1995.
- Rebai, S., H. Philip, and A. Taboada, Modern tectonic stress field in the Mediterranean region: Evidence for variation in stress directions at different scales, *Geophys. J. Int.*, **110**, 106-140, 1992.
- Rigo, A., H. Pauchet, A. Souriau, A. Grésillaud, M. Nicolas, C. Olivera, and S. Figueras, The February 1996 earthquake sequence in the eastern Pyrenees: First results, *J. Seismol.*, **1**, 3-14, 1997.
- Roure, F., and ECORS Pyrenees Team, ECORS deep seismic data and balanced cross sections: Geometric constraints on the evolution of the Pyrenees, *Tectonics*, **8**, 23-39, 1989.
- Russo, R.M., and P.G. Silver, Trench-parallel flow beneath the Nazca plate from seismic anisotropy, *Science*, **263**, 1105-1111, 1994.
- Savage, M., and P. Silver, Mantle deformation and tectonics: Constraints from seismic anisotropy in western United States, *Phys. Earth Planet.*

- Inter.*, 78, 207-227, 1993.
- Séguret, M., and M. Daignières, Crustal scale balanced cross-sections of the Pyrenees; discussion, *Tectonophysics*, 129, 303-318, 1986.
- Silver, P.G., Seismic anisotropy beneath the continents: Probing the depths of the geology, *Annu. Rev. Earth Planet. Sci.*, 24, 385-432, 1996.
- Silver, P.G., and W.W. Chan, Shear wave splitting and subcontinental mantle deformation, *J. Geophys. Res.*, 96, 16429-16454, 1991.
- Silver, P.G., and M.K. Savage, The interpretation of shear-wave splitting parameters in the presence of two anisotropic layers, *Geophys. J. Int.*, 119, 949-963, 1994.
- Soliva, J., Les déformations ductiles dans la zone axiale des Pyrénées orientales, doctorat thesis, Univ. de Montpellier II, Montpellier, France, 1992.
- Souriau, A., and M. Granet, A tomographic study of the lithosphere beneath the Pyrenees, from local and teleseismic data, *J. Geophys. Res.*, 100, 18117-18134, 1995.
- Souriau, A., and J.D. Njike-Kassala, Anisotropy beneath the North Pyrenean Fault, *Phys. Earth Planet. Inter.*, 78, 239-244, 1993.
- Tommasi, A., A. Vauchez, and R. Russo, Seismic anisotropy in oceanic basins: Resistive drag of the sublithospheric mantle?, *Geophys. Res. Lett.*, 23, 2991-2994, 1996.
- Torne, M., B. De Cabissole, R. Bayer, A. Casas, M. Daignières, and A. Rivero, Gravity constraints on the deep structures of the Pyrenean belt along the ECORS profile, *Tectonophysics*, 166, 105-116, 1989.
- Vauchez, A., and G. Barruol, Shear wave splitting in the Appalachians and the Pyrenees: Importance of the inherited tectonic fabric of the lithosphere, *Phys. Earth Planet. Inter.*, 95, 127-138, 1996.
- Vegas, R., The Valencia trough and the origin of the western Mediterranean basins, *Tectonophysics*, 203, 249-261, 1992.
- Vielzeuf, D., and J. Kornprobst, Crustal splitting and the emplacement of the Pyrenean lherzolites and granulites, *Earth Planet. Sci. Lett.*, 67, 87-96, 1984.
- Vinnik, L.P., L.I. Makeyeva, A. Milev, and A.Y. Usenko, Global patterns of azimuthal anisotropy and deformations in the continental mantle, *Geophys. J. Int.*, 111, 433-437, 1992.
- Zoback, M.L., First- and second-order patterns of stress in the lithosphere: The World Stress Map Project, *J. Geophys. Res.*, 97, 11703-11728, 1992..
- 
- G. Barruol and A. Vauchez, Laboratoire de Tectonophysique, CNRS, Université Montpellier II, 34095 Montpellier cedex 5, France. (Email: barruol@dstu.univ-montp2.fr; vauchez@dstu.univ-montp2.fr)
- A. Souriau, Laboratoire de Dynamique Terrestre et Planétaire, CNRS, 14 av Belin, 31055 Toulouse, France. (Email: souriau@pontos.cst.cnes.fr)
- J. Diaz and J. Gallart, Institut de Ciències de la Terra "Jaume Almera", CSIC, c/ Lluís Sole Sabaris, E-08028 Barcelona, Spain. (Email: jdiaz@ija.csic.es; jgallart@ija.csic.es)
- J. Tubia and J. Cuevas, Departamento de Geodinamica, Universidad del Pais Vasco, Apartado 644 48080 Bilbao, Spain.

(Received November 25, 1997; revised May 22, 1998; accepted August 14, 1998.)